2024-09-27

Wave energy extraction from rigid rectangular compound floating plates

S. Michele *School of Engineering, Computing and Mathematics*

S. Zheng *School of Engineering, Computing and Mathematics*

E. Renzi *Northumbria University*

J. Guichard *School of Engineering, Computing and Mathematics*

A. G.L. Borthwick *School of Engineering, Computing and Mathematics*

et al. *See next page for additional authors*

Recommended Citation

Michele, S., Zheng, S., Renzi, E., Guichard, J., Borthwick, A., & Greaves, D. (2024) 'Wave energy extraction from rigid rectangular compound floating plates', *Journal of Fluids and Structures*, 130. Available at: https://doi.org/10.1016/j.jfluidstructs.2024.104193

Authors

S. Michele, S. Zheng, E. Renzi, J. Guichard, A. G.L. Borthwick, and D. M. Greaves

UNIVERSITY OF PLYMOUTH

PEARL

Wave energy extraction from rigid rectangular compound floating plates

Michele, S.; Zheng, S.; Renzi, E.; Guichard, J.; Borthwick, A. G.L.; Greaves, D. M.

Published in:
Journal of Fluids and Structures

DOI:
10.1016/j.jfluidstructs.2024.104193

Publication date:
2024

Document version:
Publisher's PDF, also known as Version of record

Citation for published version (APA):
Michele, S., Zheng, S., Renzi, E., Guichard, J., Borthwick, A. G. L., & Greaves, D. M. (2024). Wave energy extraction from rigid rectangular compound floating plates. *Journal of Fluids and Structures*, *130*, Article 104193. Advance online publication. https://doi.org/10.1016/j.jfluidstructs.2024.104193

Journal of Fluids and Structures 130 (2024) 104193

Contents lists available at ScienceDirect

Journal of Fluids and Structures

journal homepage: www.elsevier.com/locate/jfs

Wave energy extraction from rigid rectangular compound floating plates

S. Michele [a,b,*], S. Zheng [c,a], E. Renzi [d], J. Guichard [a], A.G.L. Borthwick [a], D.M. Greaves [a]

[a] School of Engineering, Computing and Mathematics, University of Plymouth, Drake Circus, Plymouth PL4 8AA, UK
[b] Department of Civil Engineering and Computer Science, Università degli Studi di Roma "Tor Vergata", Via del Politecnico 1, 00133 Roma, Italy
[c] Ocean College, Zhejiang University, Zhoushan 316021, Zhejiang, China
[d] Mathematics of Complex and Nonlinear Phenomena (MCNP), Department of Mathematics, Physics and Electrical Engineering, Northumbria University, Newcastle upon Tyne NE1 8ST, UK

ARTICLE INFO

Keywords:
Fluid–structure interaction
Offshore renewable energy
Potential flow theory

ABSTRACT

We present a theoretical model to analyse the hydrodynamics of wave energy converters (WECs) comprised of three-dimensional, rigid, floating, compound rectangular plates in the open sea. The hydrodynamic problem is solved by means of Green's theorem and a free-surface Green's function. Plate motion is predicted through decomposition into rigid natural modes. We first analyse the case of a single rectangular plate and validate our model against experimental results from physical model tests undertaken in the COAST laboratory at the University of Plymouth. Then we extend our theory to complex shapes and arrays of plates and examine how the geometry, incident wave direction and power take-off (PTO) coefficient affect the response of the platform and the consequent absorbed energy.

1. Introduction

In recent years, there has been significant interest in the analysis of floating plates used for wave energy conversion (Renzi et al., 2021; Michele et al., 2020), offshore solar energy (Yang et al., 2024), and ice sheet dynamics (Meylan and Squire, 1996). Theoretical models have been developed for the hydro-elastic responses of an array of elastic plates (Peter and Meylan, 2004; Bennetts et al., 2010), rectangular plates in channels (Geng et al., 2022; Ren et al., 2024), free-floating and submerged porous bodies (Zheng et al., 2020), compound floating plates (Kabakhpasheva and Korobkin, 2002), the time-dependent transient responses of elastic plates (Montiel et al., 2012) and floating elastic plates of variable properties (Porter and Porter, 2004; Bennetts et al., 2007; Kohout et al., 2007; Singh and Gayen, 2023; Korobkin et al., 2023; Meylan et al., 2021; Michele et al., 2024). In the offshore renewable energy (ORE) sector, flexible WECs offer an effective way to increase wave power absorption. Recently, Renzi (2016) analysed a two-dimensional piezoelectric WEC and showed that the device can extract sufficient energy to drive low-power applications. Meanwhile, Michele et al. (2022, 2023) developed advanced models based on an extension of linear potential flow theory for the hydrodynamics of two-dimensional and circular flexible WECs combined with PTO units deployed under a free-floating elastic plate.

Applications of combined rectangular floating plates for wave energy extraction have not yet been fully investigated. Noad and Porter (2017) analysed the power extraction efficiency of an articulated rectangular raft using a semi-analytic theoretical model. In the present paper, we consider a complex platform geometry involving a series of localised vertical PTO cables used to extract

---

[*] Corresponding author.
E-mail address: michele@ing.uniroma2.it (S. Michele).

https://doi.org/10.1016/j.jfluidstructs.2024.104193
Received 15 May 2024; Received in revised form 25 August 2024; Accepted 20 September 2024

wave power. To study the performance of our proposed platform, we develop a mathematical model that solves the radiation and diffraction velocity potentials by means of Green's function and Green's theorem (Noblesse, 1982; Newman, 1985; Xie et al., 2018) in a similar fashion to the analysis of the ice-sheet problem by Meylan (2002). Plate response is determined from the complex amplitude of each natural mode obtained through solution of the dynamic equation. We remark that the vast majority of hydrodynamic models consider floater systems of simple geometry (e.g. circular or two-dimensional), mainly because the standard eigenfunction expansion approach can be easily applied to such simple body shapes; however, this clearly narrows the range of applications. Conversely, the theoretical model presented herein can be extended to any floating body geometry.

We further validate our theoretical model against results obtained from physical tests undertaken in the Coastal, Ocean and Sediment Transport (COAST) laboratory at the University of Plymouth. On analysing the data, we determine heave and pitch response amplitude operators of a floating rectangular barge in regular waves, and examine the influence of wave frequency. The measured barge responses match theoretical predictions, thus confirming the reliability of our model based on linear potential flow theory. Furthermore, by determining second harmonic plate displacements in regular waves we show that the presence of higher harmonics affect the barge response. We finally analyse the influence of incident wave direction, platform size and geometry on power extraction efficiency and the surrounding wave field. These factors of influence have both constructive and destructive impacts which affect key hydrodynamic properties such as the exciting force/moment, added mass/inertia, and radiation damping. Our results indicate that platform shape has a major effect on WEC hydrodynamics and the free-surface elevation field and so should be carefully analysed during the design of WECs and ORE platforms (such as hybrid floating solar farms or wind energy platforms).

2. Mathematical model

Fig. 1 depicts configurations of three-dimensional floating rigid WEC platforms comprised of rectangular plates. Specifically:

- SET 1a consists of a single rectangular plate of area $4BL$, SET 1b and SET 1c describe a platform made of two rectangular plates each of area $2BL$, whereas SET 1d represents the case of four rectangular plates each of area BL separated by distances $2l$ and $2b$. All the plates are rigidly connected to one another;
- Configurations SET 2a and SET 2c describe indented T-shaped platforms, whereas SET 2b represents a symmetric cross-shaped platform with b and l being the dimensions of the indentations;
- SET 3a and SET 3c represent C-shaped platforms, whereas the configuration SET 3b depicts a symmetrical I-shape platform with indentations each of length l.

We assume the platform draft to be much smaller than dimensions B, L, l, b and incident wavelength (Watanabe et al., 2004), such that wave forces on the vertical platform walls can be neglected at leading order. We also assume the platform to be located in open sea of very large depth, and define a Cartesian reference system with x and y-axes coincident with the undisturbed horizontal free-surface level and z-axis pointing vertically upward. The platform is connected to an idealised PTO system composed of vertical cables each located at $x = x_i$ and $y = y_i, i = 1, \ldots, I$, where I is the total number of PTOs.

The displacement of the platform is described by the following dynamic equation,

$$\mu \partial_{tt} W = q, \text{ on } S_p, \tag{1}$$

where W is the plate vertical displacement, t is time, q is the transversely distributed vertical load (positive in the z-direction), μ is the constant mass per unit wetted area of the platform, and S_p is the platform wetted surface. In defining the linearised hydrodynamic problem, it is assumed that the fluid is inviscid and the flow is irrotational, such that the velocity potential $\Phi(x, y, z, t)$ satisfies Laplace's equation

$$\nabla^2 \Phi = 0, \tag{2}$$

in the fluid domain Ω. At the free surface S_f, we apply linearised kinematic and mixed boundary conditions,

$$\partial_t \zeta = \partial_z \Phi, \quad \partial_{tt} \Phi + g \partial_z \Phi = 0, \text{ on } S_f, \tag{3}$$

where ζ is free-surface elevation and $g = 9.806$ m s^{-2} is acceleration due to gravity. We also assume negligible fluid motion at large depth, i.e.,

$$\left(\Phi, \partial_z \Phi\right) \to 0, \quad z \to -\infty. \tag{4}$$

Given that the platform draft is assumed to be much smaller than the platform horizontal dimensions, the kinematic boundary condition at the wetted surface of the platform can be Taylor-expanded about $z = 0$. The linearised condition becomes

$$\partial_z \Phi = \partial_t W, \text{ on } S_p. \tag{5}$$

We neglect initial transient motion and consider cases where the plate is forced by monochromatic incident waves of constant frequency ω and amplitude A. The following harmonic expansion applies

$$\{\Phi, \zeta, W\} = \mathrm{Re}\left\{(\phi, \eta, w) e^{-\mathrm{i}\omega t}\right\}, \tag{6}$$

in which i is the imaginary unit. Writing the governing equations and boundary equations in terms solely of spatial variables:

$$\nabla^2 \phi = 0, \qquad \text{in } \Omega, \tag{7}$$

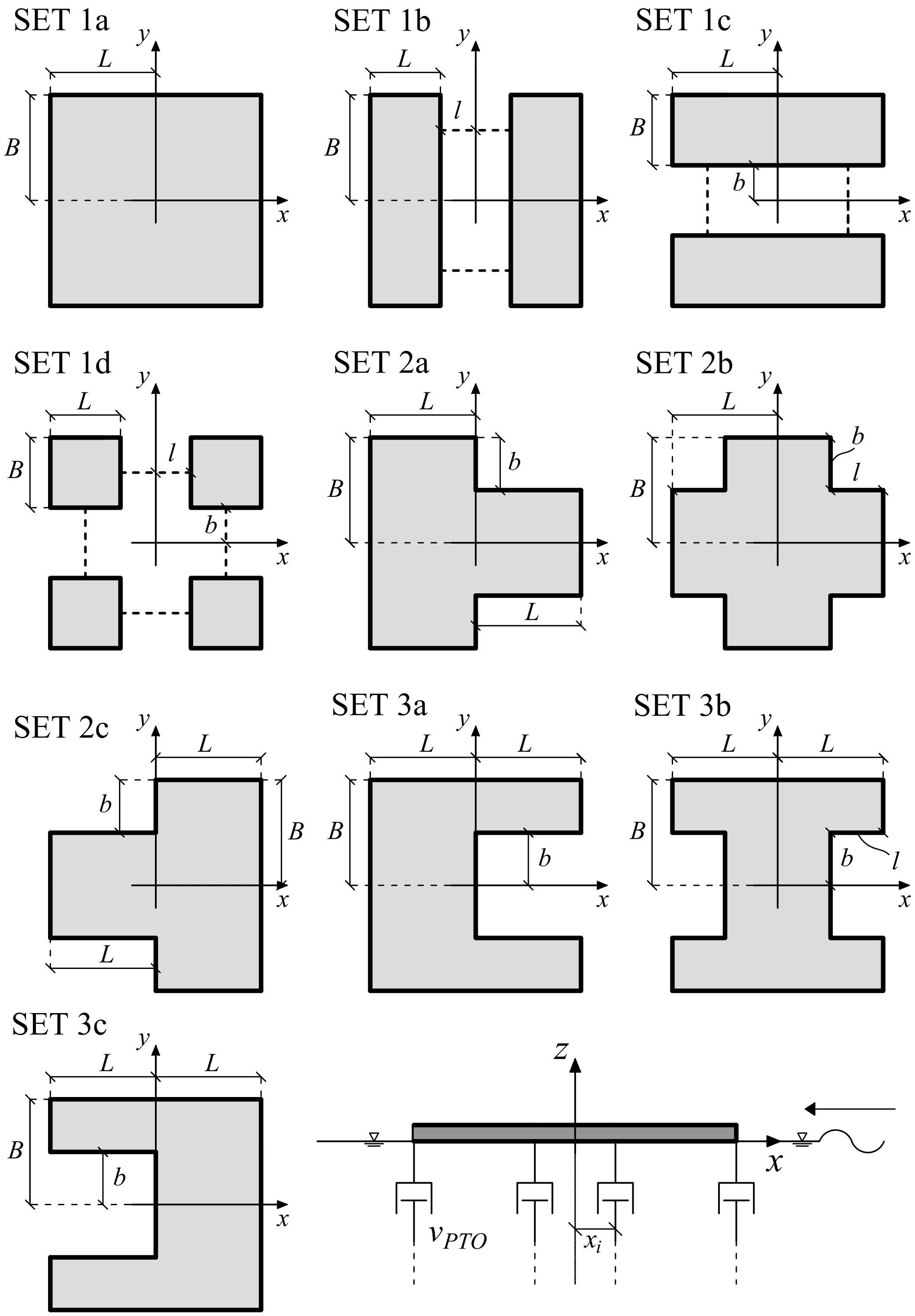

Fig. 1. View from above of all the configurations and side view of the floating platform and PTO cables.

$$\partial_z \phi = -\mathrm{i}\omega\eta, \qquad \text{on } S_f, \tag{8}$$

$$\partial_z \phi = \frac{\omega^2}{g}\phi, \qquad \text{on } S_f, \tag{9}$$

$$\partial_z \phi = -\mathrm{i}\omega w, \qquad \text{on } S_p, \tag{10}$$

$$\left(\phi, \partial_z \phi\right) \to 0, \qquad z \to -\infty. \tag{11}$$

The platforms considered herein are symmetric with respect to the x axis, and so we follow Newman (1994) and Michele et al. (2020) to decompose the displacement of the plate into heave, pitch and roll modes,

$$w = \zeta_h + \zeta_p x + \zeta_r y, \tag{12}$$

where ζ_h, ζ_p and ζ_r represent the unknown complex amplitudes for the heave, pitch and roll motions. As shown later, the mode expansion approach facilitates improved understanding of the resonance of natural modes and optimisation of power extraction efficiency.

We proceed by expanding the velocity potential ϕ in diffraction and radiation components (Mei et al., 2005):

$$\phi = \phi_D + \phi_R, \quad \phi_R = \zeta_h \phi_h + \zeta_p \phi_p + \zeta_r \phi_r, \quad \phi_D = \phi_I + \phi_S, \tag{13}$$

where

$$\phi_I = -\frac{\mathrm{i}Ag}{\omega} \mathrm{e}^{kz - \mathrm{i}k[x\cos(\Psi) + y\sin(\Psi)]}, \text{ in } \Omega, \tag{14}$$

is the incident velocity potential, Ψ is the incidence angle, $k = \omega^2/g$ is the wavenumber satisfying the dispersion relation for deep-water waves, ϕ_S is scattering velocity potential, ϕ_D is diffraction velocity potential, ϕ_R is total radiation velocity potential, and ϕ_h, ϕ_p, ϕ_r are heave, pitch and roll velocity potentials. The corresponding radiation and scattering boundary value problems are given by

$$\nabla^2 \phi_{S,R} = 0, \qquad \text{in } \Omega, \tag{15}$$

$$g\partial_z \phi_{S,R} - \omega^2 \phi_{S,R} = 0, \qquad \text{on } S_f, \tag{16}$$

$$\partial_z \phi_S = -\partial_z \phi_I, \qquad \text{on } S_p, \tag{17}$$

$$\partial_z \phi_R = -\mathrm{i}\omega w, \qquad \text{on } S_p, \tag{18}$$

$$\left(\phi_{S,R}, \partial_z \phi_{S,R}\right) \to 0, \qquad z \to -\infty. \tag{19}$$

Finally we require the velocity potential $\phi_{S,R}$ to be outgoing for $\mathcal{R} = \sqrt{x^2 + y^2} \to \infty$, i.e.,

$$\lim_{\mathcal{R}\to\infty} \sqrt{\mathcal{R}} \left(\partial_{\mathcal{R}} - \mathrm{i}k\right) \phi_{S,R} = 0, \tag{20}$$

at large distance from the platform. Solution of (15)–(20) can be found via Green's theorem and Green's function G as given by Meylan (2002), Newman (1985) and Linton and McIver (2001). We obtain

$$\phi_{S,R}(x, y, z) = \int_{S_p} \left(\partial_z \phi_{S,R} - k\phi_{S,R}\right) G(x, y, z; x', y')\, \mathrm{d}x'\mathrm{d}y', \tag{21}$$

where

$$\begin{aligned} G(x, y, z; x', y') &= \frac{1}{2\pi} \int_0^\infty \frac{e^{Kz} K J_0(KR)}{(K-k)}\, \mathrm{d}K = \frac{1}{2\pi}\left[\frac{1}{r} + \int_0^\infty \frac{e^{Kz} k J_0(KR)}{(K-k)}\, \mathrm{d}K\right], \\ &= \frac{1}{2\pi r} - \frac{k e^{kz}}{4}\left[Y_0(kR) + \mathcal{H}_0(kR) - 2\mathrm{i}J_0(kR)\right] - \frac{k e^{kz}}{2\pi} \int_{kz}^0 \frac{e^{-\tau}}{\sqrt{\tau^2 + (kR)^2}}\, \mathrm{d}\tau, \end{aligned} \tag{22}$$

$r = \sqrt{(x - x')^2 + (y - y')^2 + z^2}$ is the distance from the source point to the point of interest, $R = r|_{z=0} = \sqrt{(x - x')^2 + (y - y')^2}$, J_0 and Y_0 are the Bessel functions of first and second kind and order zero, whereas $\mathcal{H}_0$ is the Struve function of order zero (Gradshteyn and Ryzhik, 2007). The expression above contains explicitly the singular term $1/r$ and thus facilitates the numerical computations (Newman, 1985). We recall that the floating platform has zero draft, and so the Fredholm integral Eq. (21) does not possess irregular frequencies (Mei et al., 2005), thus providing a computational advantage. Furthermore, solution of the equation of motion of the plate will require evaluation of ϕ on the platform surface S_p. In this case expressions (21)–(22) give

$$\phi_{S,R}(x, y, 0) = \int_{S_p} \left(\partial_z \phi_{S,R} - k\phi_{S,R}\right) \left\{\frac{1}{2\pi R} - \frac{k}{4}\left[Y_0(kR) + \mathcal{H}_0(kR) - 2\mathrm{i}J_0(kR)\right]\right\} \mathrm{d}x'\mathrm{d}y'. \tag{23}$$

The Neumann condition $\partial_z \phi_{S,R}$ is known, therefore Eq. (23) can be resolved by dividing the surface S_p into discrete panels, and approximating the velocity potential in each panel by a constant ϕ_{mn} and then solving numerically the corresponding non-homogeneous linear system for ϕ_{mn}, $m = 1, \ldots, M$, $n = 1, \ldots, N$, where $(N \times M)$ is the number of panels, $\phi_{nm} = \phi(x_m, y_n)$, and (x_m, y_n) is the coordinate of the centre of each panel. In addition, we approximate the Green's function for small R when (x, y) and (x', y') are located on the same grid element and carry out the integration analytically. By assuming a rectangular panel of size $\Delta X \Delta Y$ we first get

$$\mathcal{I} = \int_{y-\Delta Y/2}^{y+\Delta Y/2} \int_{x-\Delta X/2}^{x+\Delta X/2} \frac{1}{R}\mathrm{d}x'\mathrm{d}y' = \int_{y-\Delta Y/2}^{y+\Delta Y/2} \log\left(\frac{\Delta X + \sqrt{\Delta X^2 + 4(y - y')^2}}{-\Delta X + \sqrt{\Delta X^2 + 4(y - y')^2}}\right)\mathrm{d}y'$$

$$= 2\left[\Delta Y \log\left(\frac{\Delta X + \sqrt{\Delta X^2 + \Delta Y^2}}{\Delta Y}\right) + \Delta X \log\left(\frac{\Delta Y + \sqrt{\Delta X^2 + \Delta Y^2}}{\Delta X}\right)\right], \tag{24}$$

then recognising the dominant behaviour $G \sim 1/(2\pi R)$ for $R \to 0$, and using (24) we obtain Eq. (23) in discrete form

$$\phi_{mn} = \frac{\mathcal{I}}{2\pi}\left(\partial_z \phi_{mn} - k\phi_{mn}\right) + \sum_{p=1}^{M}\sum_{q=1}^{N} G(x_m, y_n, 0; x'_p, y'_q)\left(\partial_z \phi_{pq} - k\phi_{pq}\right)\Delta X \Delta Y \epsilon_{pq}, \tag{25}$$

where $\epsilon_{pq} = 0$ if $(p, q) = (m, n)$ and equal to unity otherwise. As also shown in Appendix, the converged solution was calculated for 1000 panels. Alternative approaches based on the Fourier transform (Porter, 2016; Noad and Porter, 2017; Porter, 2019) could also be used of course. The hypersingular integral equation approach is also suitable for the similar problem of a submerged plate (Martin and Farina, 1997; Farina and Martin, 1998; Renzi and Dias, 2012; Michele et al., 2016a; Liang et al., 2021, 2022). Once ϕ_{mn} was found on S_p we derived the velocity potential at any point in the fluid domain using Eq. (21).

2.1. Dynamic response

In the presence of all external forces, the dynamic Eq. (1) is

$$\mu \partial_{tt} W = -\rho \partial_t \Phi - \rho g W - \nu_{PTO} \partial_t W \sum_{i=1}^{I} \delta(x - x_i)\delta(y - y_i), \tag{26}$$

where ρ is fluid density, δ is the Dirac Delta function and ν_{PTO} is PTO damping coefficient. The first term on the right-hand side represents the dynamic pressure exerted by the wave field, the second term represents the hydrostatic pressure due to platform displacement, and the third term denotes the damping effect of the PTO cables in (x_i, y_i), $i = 1, \dots, I$. Using both the harmonic expansion (6) and mode decomposition (12), we obtain after some manipulation,

$$\begin{aligned} &- \mathrm{i}\omega\rho(\zeta_h \phi_h + \zeta_p \phi_p + \zeta_r \phi_r) + \left(\zeta_h + \zeta_p x + \zeta_r y\right)\left\{\rho g - \mu\omega^2 - \mathrm{i}\omega\nu_{PTO}\sum_{i=1}^{I}\delta(x - x_i)\delta(y - y_i)\right\} \\ &= \mathrm{i}\omega\rho\phi_D. \end{aligned} \tag{27}$$

The complex modal amplitudes ζ_h, ζ_p and ζ_r are found by multiplying both sides of (27) by each of the modal shape functions $(1, x, y)$ and then integrating over the platform surface S_p (Michele et al., 2023; Newman, 1994). Assuming for simplicity a PTO distribution that is symmetrical with respect to the x and y axes, and noting the x-symmetric shape of the platforms in Fig. 1, we obtain

$$\zeta_h = \frac{1}{D}\left\{F_h C_{pp} - F_p C_{ph} - \omega\left\{\mathrm{i}\left[F_h(\lambda_{pp} + \nu_{pp}) - F_p \lambda_{ph}\right] + \omega\left[F_h(\mu_{pp} + I_{pp}) - F_p(\mu_{ph} + I_{ph})\right]\right\}\right\}, \tag{28}$$

$$\zeta_p = \frac{1}{D}\left\{F_p C_{hh} - F_h C_{ph} - \omega\left\{\mathrm{i}\left[F_p(\lambda_{hh} + \nu_{hh}) - F_h \lambda_{ph}\right] + \omega\left[F_p(\mu_{hh} + I_{hh}) - F_h(\mu_{ph} + I_{ph})\right]\right\}\right\}, \tag{29}$$

$$\zeta_r = \frac{F_r}{C_{rr} - \omega\left[\mathrm{i}(\lambda_{rr} + \nu_{rr}) + \omega(\mu_{rr} + I_{rr})\right]}, \tag{30}$$

where the subscripts p, h, r refer to pitch, heave and roll,

$$\begin{aligned} D = &\left\{C_{hh} - \omega\left[\mathrm{i}(\lambda_{hh} + \nu_{hh}) + (\mu_{hh} + I_{hh})\omega\right]\right\}\left\{C_{pp} - \omega\left[\mathrm{i}(\lambda_{pp} + \nu_{pp}) + (\mu_{pp} + I_{pp})\omega\right]\right\} \\ &- \left\{C_{ph} - \omega\left[\mathrm{i}\lambda_{ph} + (\mu_{ph} + I_{ph})\omega\right]\right\}^2, \end{aligned} \tag{31}$$

is the denominator,

$$F_h = \mathrm{i}\omega\rho \int_{S_p} \phi_D \,\mathrm{d}S_p, \quad F_p = \mathrm{i}\omega\rho \int_{S_p} x\phi_D \,\mathrm{d}S_p, \quad F_r = \mathrm{i}\omega\rho \int_{S_p} y\phi_D \,\mathrm{d}S_p, \tag{32}$$

are the heave force and pitch and roll moments,

$$C_{hh} = \rho g \int_{S_p} \mathrm{d}S_p, \quad I_{hh} = \mu \int_{S_p} \mathrm{d}S_p, \quad \mu_{hh} = \frac{1}{\omega^2}\mathrm{Re}\left\{\mathrm{i}\omega\rho \int_{S_p} \phi_h \,\mathrm{d}S_p\right\}, \tag{33}$$

$$C_{pp} = \rho g \int_{S_p} x^2 \,\mathrm{d}S_p, \quad I_{pp} = \mu \int_{S_p} x^2 \,\mathrm{d}S_p, \quad \mu_{pp} = \frac{1}{\omega^2}\mathrm{Re}\left\{\mathrm{i}\omega\rho \int_{S_p} x\phi_p \,\mathrm{d}S_p\right\}, \tag{34}$$

$$C_{ph} = \rho g \int_{S_p} x \,\mathrm{d}S_p, \quad I_{ph} = \mu \int_{S_p} x \,\mathrm{d}S_p, \quad \mu_{ph} = \frac{1}{\omega^2}\mathrm{Re}\left\{\mathrm{i}\omega\rho \int_{S_p} \phi_p \,\mathrm{d}S_p\right\}, \tag{35}$$

$$C_{rr} = \rho g \int_{S_p} y^2 \mathrm{d}S_p, \quad I_{rr} = \mu \int_{S_p} y^2 \mathrm{d}S_p, \quad \mu_{rr} = \frac{1}{\omega^2}\mathrm{Re}\left\{\mathrm{i}\omega\rho \int_{S_p} y\phi_r \,\mathrm{d}S_p\right\}, \tag{36}$$

are the restoring forces, inertia and added masses, and

$$\nu_{hh} = N\nu_{PTO},\ \lambda_{hh} = \mathrm{Im}\left\{\mathrm{i}\rho\int_{S_p}\phi_h\,\mathrm{d}S_p\right\},\ \nu_{pp} = \nu_{PTO}\sum_{n=1}^{N}x_n^2, \tag{37}$$

$$\lambda_{pp} = \mathrm{Im}\left\{\mathrm{i}\rho\int_{S_p}x\phi_p\,\mathrm{d}S_p\right\},\ \lambda_{ph} = \mathrm{Im}\left\{\mathrm{i}\rho\int_{S_p}\phi_p\,\mathrm{d}S_p\right\}, \tag{38}$$

$$\nu_{rr} = \nu_{PTO}\sum_{n=1}^{N}y_n^2,\ \lambda_{rr} = \mathrm{Im}\left\{\mathrm{i}\rho\int_{S_p}y\phi_r\,\mathrm{d}S_p\right\}, \tag{39}$$

represent radiation damping and PTO damping. The pitch and heave modes are coupled with one another through the non-symmetry of the platform geometry with respect the y-axis, i.e., through non-diagonal terms related to the restoring force C_{ph}, added mass μ_{ph}, and radiation damping λ_{ph}. In the configurations SET 1, SET 2b and SET 3b these terms are identically equal to zero. Note that the roll mode is decoupled because of symmetry of both platform geometry and PTO distribution with respect the x-axis.

Corresponding eigenfrequencies are readily evaluated by equating to zero the determinants of the inertia and restoring force matrices. This leads to the following eigenvalue condition for heave and pitch (Michele et al., 2016a)

$$\begin{aligned}&\omega^4\left[(\mu_{hh}+I_{hh})(\mu_{pp}+I_{pp})-(\mu_{ph}+I_{ph})^2\right]+C_{hh}C_{pp}-C_{ph}^2\\&-\omega^2\left[C_{pp}(\mu_{hh}+I_{hh})-2C_{ph}(\mu_{ph}+I_{ph})+C_{hh}(\mu_{pp}+I_{pp})\right]=0,\end{aligned} \tag{40}$$

whereas the eigenfrequency of the roll mode is readily given by

$$\omega_{roll} = \sqrt{\frac{C_{rr}}{\mu_{rr}+I_{rr}}}. \tag{41}$$

Expression (40) highlights the effect of mode coupling on each eigenfrequency. In the case of a symmetric platform, the dry modes are fully decoupled with one another, therefore expressions (28), (29) and (40) become

$$\zeta_h = \frac{F_h}{C_{hh}-\omega\left[\mathrm{i}(\lambda_{hh}+\nu_{hh})+\omega(\mu_{hh}+I_{hh})\right]},\ \zeta_p = \frac{F_p}{C_{pp}-\omega\left[\mathrm{i}(\lambda_{pp}+\nu_{pp})+\omega(\mu_{pp}+I_{pp})\right]}, \tag{42}$$

$$\left[C_{hh}-\omega^2(\mu_{hh}+I_{hh})\right]\left[C_{pp}-\omega^2(\mu_{pp}+I_{pp})\right]=0, \tag{43}$$

which gives the eigenfrequencies for heave and pitch

$$\omega_{heave} = \sqrt{\frac{C_{hh}}{\mu_{hh}+I_{hh}}},\quad \omega_{pitch} = \sqrt{\frac{C_{pp}}{\mu_{pp}+I_{pp}}}. \tag{44}$$

For simplicity, let us now consider a symmetrical PTO system made up of four cables at the four plate corners, i.e., at $x_i = \pm L$, $y_i = \pm B$ for SET 1a and SET 3, $x_i = \pm(L+l)$, $y_i = \pm B$ for SET 1b, $x_i = \pm L$, $y_i = \pm(B+b)$ for SET 1c, $x_i = \pm(L+l)$, $y_i = \pm(B+b)$ for SET 1d, and $x_i = \pm L$, $y_i = \pm(B-b)$ for the remaining platform configurations SET 2. Given the mode responses (28)–(29), the average power generated by the platform is

$$P = 2\nu_{PTO}\omega^2\left[\left|\zeta_h\right|^2+(L+\alpha l)^2\left|\zeta_p\right|^2+(B+\beta b)^2\left|\zeta_r\right|^2\right], \tag{45}$$

where $\alpha = 1$ for SET 1b, SET 1d and equal to zero for the remaining cases; $\beta = 1$ for SET 1c and SET 1d, $\beta = -1$ for SET 2 and $\beta = 0$ for the other platform configurations. Platform efficiency is represented by the capture-width ratio (Mei et al., 2005)

$$C_W = \frac{P}{\rho g A^2 C_g B},\quad C_g = \frac{\omega}{2k}, \tag{46}$$

where $\rho g A^2 C_g B$ is energy flux per platform width ($2B$), and C_g is wave group velocity in deep water. The foregoing expressions will be used later in Section 4 to assess the power extraction efficiency of the platform.

3. Experimental set-up and validation of theoretical model

Physical model tests were undertaken on a floating rectangular plate in water waves in the COAST laboratory at the University of Plymouth. The COAST Ocean basin is of length 35 m and width 15.5 m, and has a movable floor that accommodates an operating depth of up to 3 m. Water waves are generated by 24 individually controlled, hinged-flap, wave-absorbing paddles.

The plate was fabricated from timber whose elastic deformation was low-amplitude in accordance with the theoretical model developed in Section 2. To avoid strong wave interactions with the lateral basin walls, the plate width $2B = 0.86$ m and plate length $2L = 2.319$ m were selected to be much smaller than the basin horizontal dimensions. The mass of the plate was determined experimentally as 83.8 kg. The negligible plate draft of 0.042 m and $\mu = 42$ kg m^2 were again in keeping with the theoretical model discussed in Section 2.

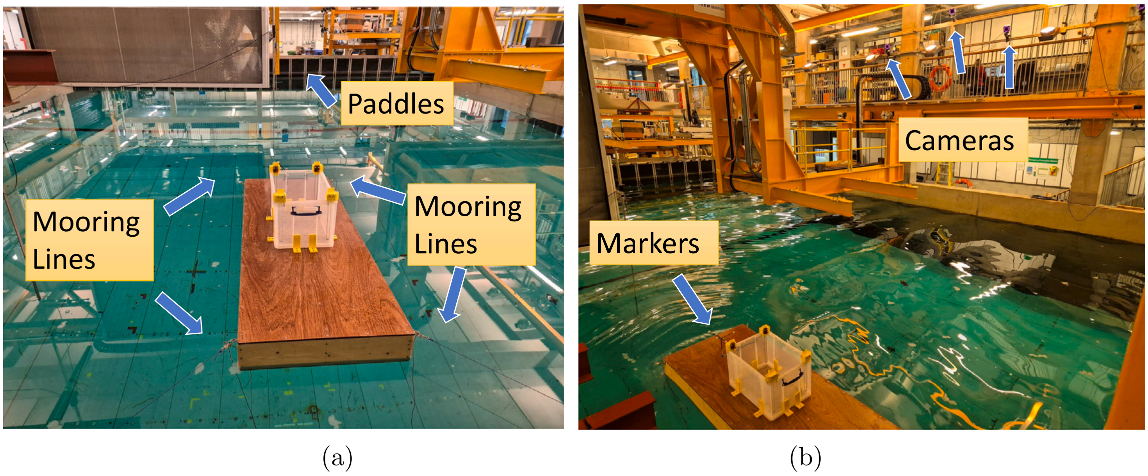

Fig. 2. View of the experimental set-up, markers, cameras, and mooring lines connected to the basin walls. The rectangular barge is placed in front of the paddles, with each mooring line located at 45 ° with respect to the direction of incident wave propagation x. Three of the six cameras used for motion tracking are located at the top-right of the photograph. The five markers are indicated at the top of the barge. The empty container on top of the barge was set up in preparation for an alternative study; it has negligible weight and does not affect the overall dynamics.

To prevent second-order plate drift, four horizontal moorings, each of length ∼10.3 m were connected to vertical beams fixed to the basin walls (see Fig. 2). The mooring line was set at an angle of 45 ° with respect to the incident wave direction, permitting symmetric pitch and heave response. Each mooring was fitted with an end spring of stiffness 596 N m^{-1} that avoided the occurrence of impulsive forces (unaccounted for in the theoretical model). As is shown in the next subsection, we observed plate vertical oscillations of the order $O(1)$ cm; hence, given the length of the mooring line, we get that the effect of mooring forces on heave and pitch can be neglected at leading order. This finding is in agreement with our theoretical model.

Plate movement was recorded by a motion tracking device developed by QUALISYS to an accuracy of $O(10^{-3})$ m. Plate displacements were sampled at a frequency of 128 Hz, and response amplitude operators for heave and pitch then determined using MATLAB. Fig. 2(b) shows the location of three of the six cameras placed above the basin to capture the three-dimensional positions of markers. Each marker comprised a 30 mm diameter polystyrene sphere covered with retro-reflective tape and was rigidly connected to the top surface of the plate. Plate motion was excited by incident waves whose direction was parallel to the x-axis in order to produce a symmetric response in heave and pitch. A total of 5 markers were fixed to the plate, all of which were visible at all times to the six cameras.

3.1. Test summary

A series of tests were undertaken to investigate synchronous plate responses to monochromatic regular waves of constant amplitude $A = 0.02$ m. Data were collected for different fundamental wave frequencies in the range $f \in [0.3; 1.5]$ Hz with frequency increment $\Delta f = 0.05$ Hz. The basin water depth was set to $h = 3$ m corresponding to deep-water conditions throughout the wave frequency range considered. Fourier analysis was used to derive the experimental response amplitude operators (RAOs) from the measured plate-displacement time series. Following Mei (1997) we utilise the Fourier series expansion,

$$\psi = \frac{a_0}{2} + \sum_{n=1}^{\infty} \left(a_n \cos\left[\frac{n\pi(2t - t_2 - t_1)}{t_2 - t_1}\right] + b_n \sin\left[\frac{n\pi(2t - t_2 - t_1)}{t_2 - t_1}\right] \right), \tag{47}$$

where ψ refers to the recorded time series of displacement in heave or pitch, and the parameters (t_1, t_2) define the start and end of the recorded time interval. The Fourier coefficients a_n, b_n, for $n \geq 1$, represent plate oscillations and are evaluated from the integral relationships,

$$a_n = \frac{2}{t_2 - t_1} \int_{t_1}^{t_2} \psi(t) \cos\left[\frac{n\pi(2t - t_2 - t_1)}{t_2 - t_1}\right] \mathrm{d}t, \tag{48}$$

$$b_n = \frac{2}{t_2 - t_1} \int_{t_1}^{t_2} \psi(t) \sin\left[\frac{n\pi(2t - t_2 - t_1)}{t_2 - t_1}\right] \mathrm{d}t. \tag{49}$$

The generalised raw response amplitude spectrum is given by

$$\mathcal{A}_n = \sqrt{a_n^2 + b_n^2}. \tag{50}$$

The plate response at leading order is synchronous with the incident wave frequency; hence the nth component is extracted from the amplitude spectrum (50), such that $n = \lfloor f(t_2 - t_1) \rceil$, where f is the assigned incident wave frequency and $\lfloor\ \rceil$ denotes the closest

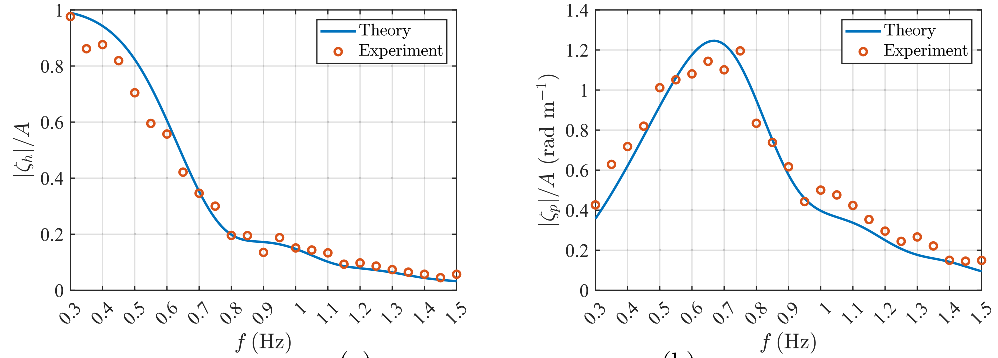

(a) (b)

Fig. 3. Response amplitude operator versus fundamental incident wave frequency for (a) heave, and (b) pitch. Solid lines show the analytical solutions (28)–(29), and symbols represent the experimental results.

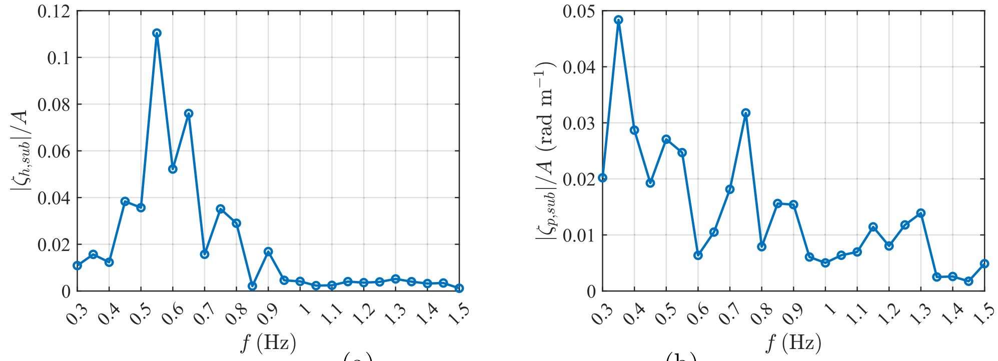

(a) (b)

Fig. 4. Normalised second-harmonic response contributions versus fundamental incident wave frequency for (a) heave, and (b) pitch.

integer. We consider a time interval of 80 s from $t_1 = 80$ s to $t_2 = 160$ s, during which steady state has been reached and transient effects from the initial wave front and trailing waves can be neglected. Experimental values of the heave and pitch RAOs were evaluated by dividing the spectral components by the recorded incident wave amplitude

Fig. 3 depicts the measured and theoretical heave and pitch response amplitude operators as functions of fundamental wave frequency. Bearing in mind the limitations of the theoretical model, good agreement is achieved between (28) and (29) and the corresponding experimental values denoted by red circles. This indicates that the theoretical model properly captures the overall heave and pitch behaviour of the rigid plate in waves.

We now evaluate the plate second-harmonic response in monochromatic waves. Using a perturbation approach, nonlinear terms lead to contributions of order $O(Ak)$ and smaller (Mei et al., 2005). In our tests $O(Ak) \ll 1$, and so the second-harmonic responses are likely to be less pronounced than the linear synchronous behaviour. Following Michele et al. (2023), we use Fourier analysis to obtain the second-harmonic response component for incident waves of index $n = \lfloor 2f(t_2 - t_1) \rfloor$. Herein, the response amplitude operators of the second subharmonic in heave and pitch are denoted $\zeta_{h,sub}$ and $\zeta_{p,sub}$.

Fig. 4 displays the measured second-harmonic RAOs as functions of incident wave frequency. The second-harmonic responses in heave and pitch are significantly smaller than the corresponding linear responses depicted in Fig. 3. This is because the second-harmonics are at most $O(Ak)$ order effects and the wave steepness is very small in this case. Even so, as shown in Fig. 4(a), the second harmonic component can be important as evidenced by $|\zeta_{h,sub}|/A$ approaching ~0.12 for incident wave frequency $f = 0.55$ Hz. This peak warrants further theoretical investigation through weakly nonlinear approaches.

4. Results and discussion

In this section we examine the effects of plate geometry, PTO coefficient, incident wave direction and wave frequency on the hydrodynamic behaviour and energy extraction efficiency of the floating platforms shown in Fig. 1. For brevity, we consider the following fixed parameters: wave amplitude $A = 1$ m, water density $\rho = 1000$ kg m^{-3}, platform mass per unit area $\mu = 44$ kg m^{-2}, and platform length $L = 5$ m. The value of μ is the same as adopted by Michele et al. (2024, 2020) enabling comparison against their results.

Table 1
First eigenfrequencies (rad/s) in heave, pitch and roll for plate width $B = [L/2; L; 2L]$. $B \to \infty$ corresponds with the two-dimensional model of Michele et al. (2020).

Plate width	Heave	Pitch	Roll
$B = L/2$	2.40 (rad/s)	2.77 (rad/s)	3.35 (rad/s)
$B = L$	1.92 (rad/s)	2.51 (rad/s)	2.51 (rad/s)
$B = 2L$	1.72 (rad/s)	2.41 (rad/s)	1.99 (rad/s)
$B \to \infty$	1.63 (rad/s)	2.34 (rad/s)	0 (rad/s)

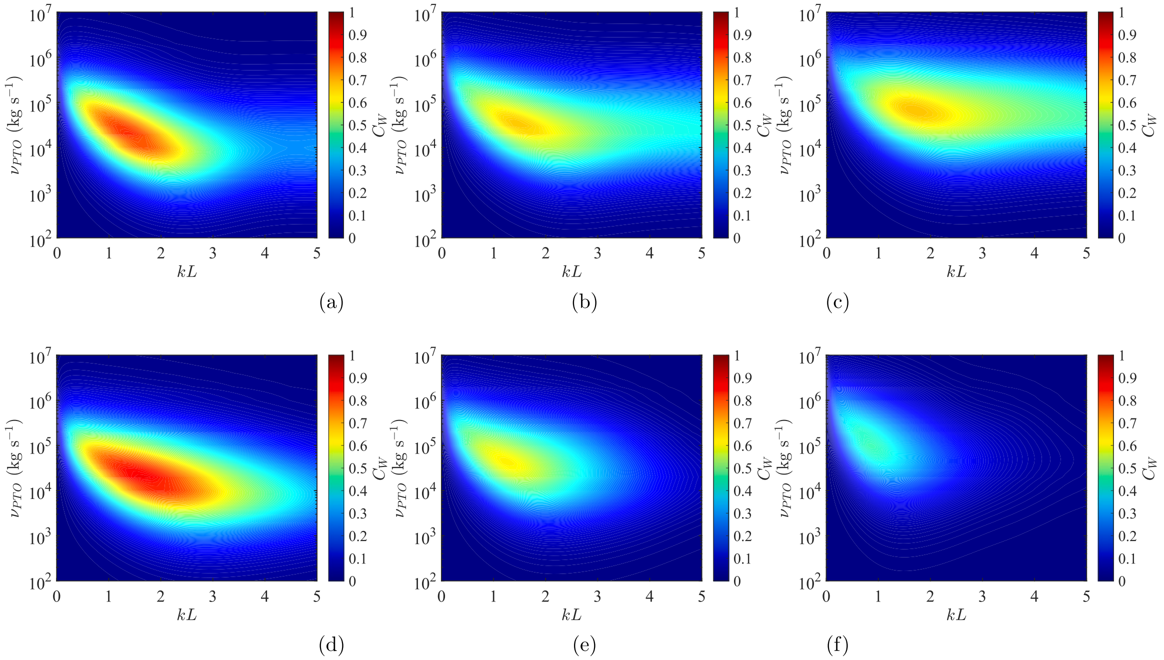

(a) (b) (c)

(d) (e) (f)

Fig. 5. Capture-width ratio C_W as a function of angle of incidence Ψ, kL and PTO coefficient ν_{pto} for the single plate case SET 1a. Plate length is $L = 5$ m, and: (a) $B = L/2$, $\Psi = 0$ rad, (b) $B = L$, $\Psi = 0$ rad, (c) $B = 2L$, $\Psi = 0$ rad, (d) $B = L/2$, $\Psi = \pi/4$ rad, (e) $B = L$, $\Psi = \pi/4$ rad, and (f) $B = 2L$, $\Psi = \pi/4$ rad.

4.1. SET 1a: Single rectangular plate

We first examine the effect of the relative horizontal dimensions of a single rectangular plate on its power extraction efficiency. We consider three values of plate width $B = [L/2; L; 2L]$, for which the eigenfrequencies are evaluated by solving (40) and (41). Table 1 lists the numerical values of the eigenfrequencies, where $B \to \infty$ refers to values from the two-dimensional model developed by Michele et al. (2020). It can be seen that the eigenfrequencies tend to those of the two-dimensional case for increasing B/L ratio.

Fig. 5 presents contour plots of capture-width ratio (46) as a function of kL and PTO coefficient ν_{PTO} for two values of wave incidence angle $\Psi = (0, \pi/4)$ rad. It can be seen that C_W invariably has a single visible peak due to the presence of two resonant frequencies. This maximum is shifted towards frequencies smaller than those listed in Table 1 because of PTO and radiation damping effects, in a similar fashion to a damped harmonic oscillator. The absolute maximum of C_W decreases and the efficiency bandwidth grows as the plate width increases. Therefore potential positive benefits on reduction of construction costs are possible because the economic viability and lifespan of WECs depend also on their size. This behaviour is different from that of a hinged vertical plate oscillating in pitch, where increasing the width does not change sensibly C_W (Renzi and Dias, 2013). Therefore, systematic alteration of the plate dimensions and configuration during the analysis stage allows designers to optimise the plate WEC for different broadband sea-states and to maximise corresponding energy extraction efficiency while reducing cost. Even so, designers should consider the effect of plate width on plate structural resistance, which could penalise the overall behaviour of an actual device in the open ocean. Larger plate dimensions induce greater wave loads and may render the device less durable.

In the case of oblique waves (Figs. 5(d)–5(f)), we note that for $B < L$ the capture-width ratio tends to improve and the generated power by the plate increases. On the contrary, for $B \geq L$, oblique waves are associated with lower energy production as has also been previously shown for arrays of OWSCs (Michele et al., 2016b). This is primarily because the platform exposure to incident waves depends on Ψ.

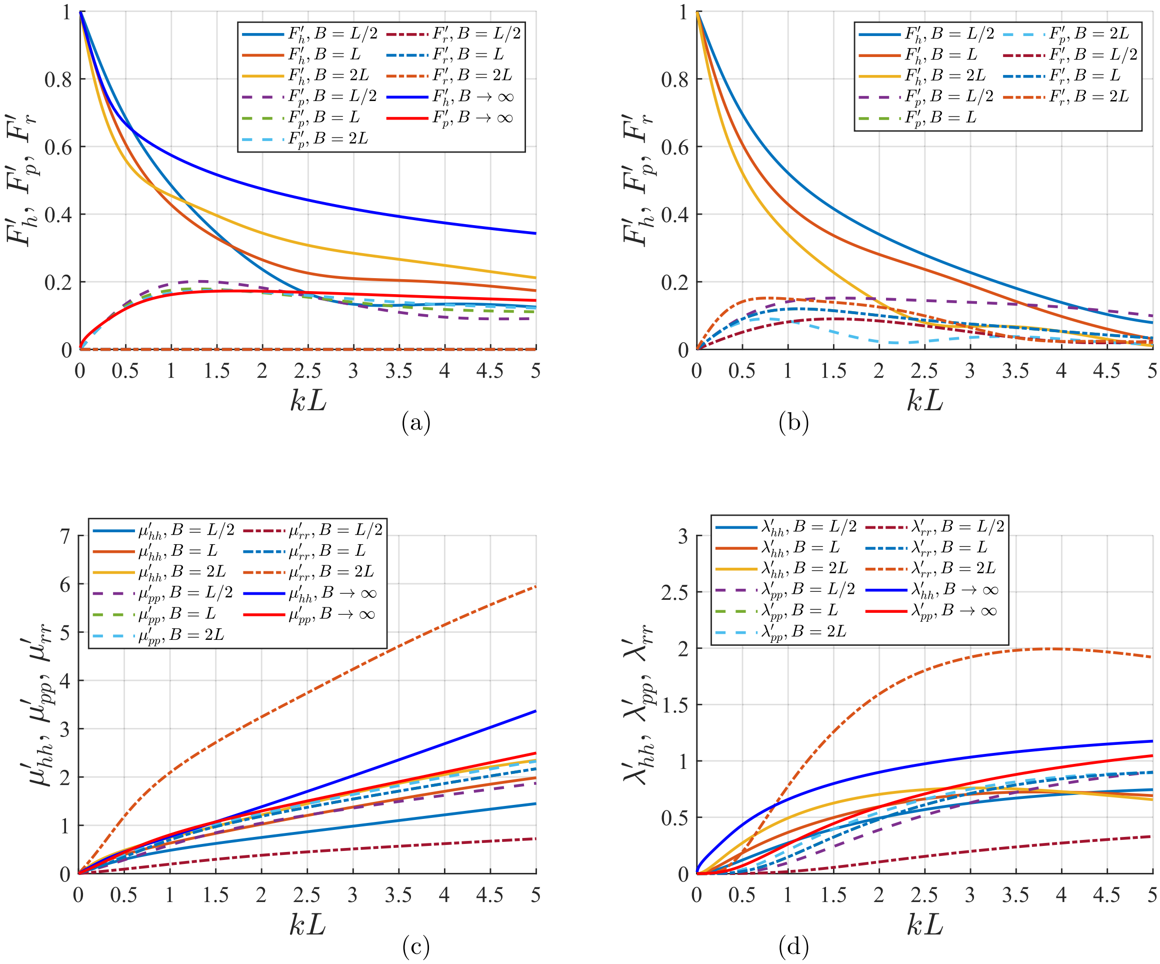

Fig. 6. Exciting and radiation force components plotted against kL for a rectangular plate with $B/L = [1/2; 1; 2; \infty]$. (a) heave exciting force, pitch and roll exciting moments, $\Psi = 0$ rad; (b) heave exciting force, pitch and roll exciting moments, $\Psi = \pi/4$ rad; (c) heave added mass, pitch and roll added inertia; (d) heave, pitch and roll radiation damping.

Fig. 6 shows the behaviour of non-dimensional exciting forces/moment, added mass/inertia and radiation damping, defined as

$$\begin{aligned} F'_h &= \frac{F_h}{A_p \rho g A}, \quad F'_p = \frac{F_p}{4B(L+l\alpha)^2 \rho g A}, \quad F'_r = \frac{F_r}{4L(B+b\gamma)^2 \rho g A} \\ \mu'_{hh} &= \frac{\mu_{hh}\omega^2}{4BL\rho g}, \quad \mu'_{pp} = \frac{\mu_{pp}\omega^2}{\rho g 4B(L+l\alpha)^2}, \quad \mu'_{rr} = \frac{\mu_{rr}\omega^2}{\rho g 4L(B+b\gamma)^2}, \\ \lambda'_{hh} &= \frac{\lambda_{hh}\omega}{4BL\rho g}, \quad \lambda'_{pp} = \frac{\lambda_{pp}\omega}{4B(L+l\alpha)^2 \rho g}, \quad \lambda'_{rr} = \frac{\lambda_{rr}\omega}{4L(B+b\gamma)^2 \rho g}, \end{aligned} \tag{51}$$

versus non-dimensional kL for $B = [L/2, L, 2L]$ and $B \to \infty$, where $\gamma = 1$ for SET 1c and SET 1d and equal to zero for all the other cases considered. In defining (51), A_p is used to indicate the platform wetted area. The hydrodynamic forces on the two-dimensional plate are calculated in a similar fashion by dividing the denominators in (51) by $2B$, i.e., by reference to a plate of unit width. We note that the hydrodynamic heave force F_h decreases with wave frequency, and tends to the hydrostatic value $\rho g A_p$ as $\omega \to 0$. The pitch force tends to zero as the wave frequency tends to zero and has a maximum at $kL \simeq \pi/2$, i.e., when the wavelength is four times the plate length L. As B/L increases, the curves approach the two-dimensional results of Michele et al. (2020). Furthermore we note that for $\Psi = \pi/4$ rad, there is an increase in heave force for $B = L/2$ and decrease for $B = 2L$. This justifies the behaviour of wave energy production shown in Fig. 5 and highlights the role of the hydrodynamic forces/moments $F_{h,p,r}$ on energy extraction efficiency. Also, the pitching moment obviously decreases with Ψ, whereas the roll moment differs from zero only for $\Psi > 0$ and the results are comparable in order of magnitude with the pitching moment in the case $\Psi = \pi/4$ rad. We point out that similar results were obtained by Porter (2016), further validating the present model.

To further examine the hydrodynamics of single rectangular plates in waves, we consider shaded spatial distributions of the normalised amplitude of diffracted free surface elevation $|\eta_D|/A$, where $\eta_D = \mathrm{i}k/\omega(\phi_I + \phi_S)_{z=0}$. Here, the subplots in Fig. 7 refer

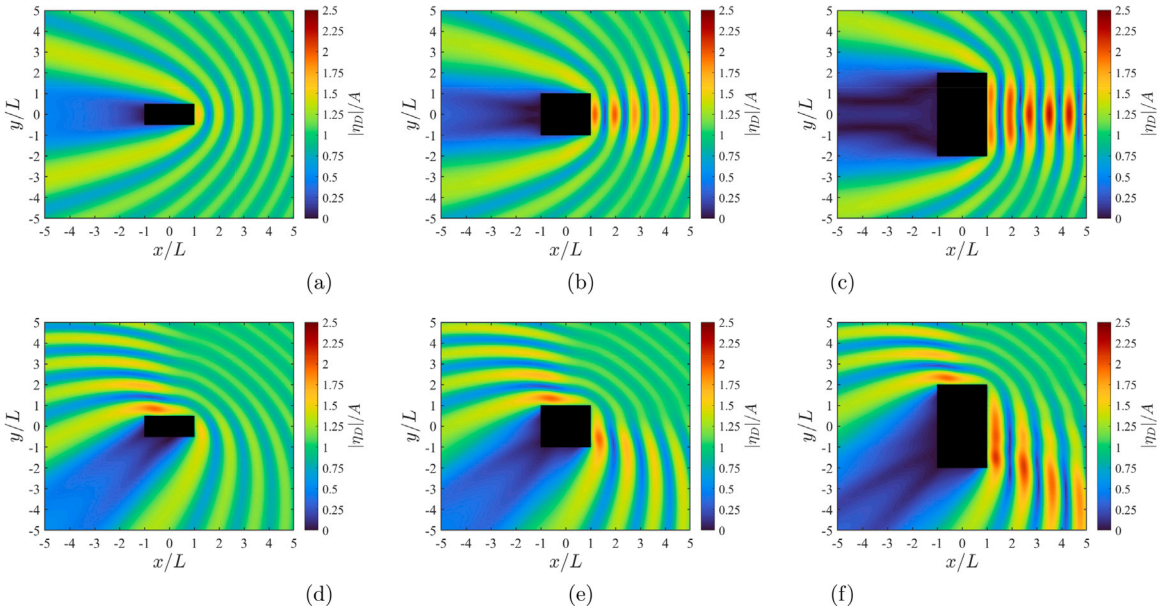

Fig. 7. Contour plots of the spatial distribution of the non-dimensional modulus of diffracted wave elevation for an incident wave of unit amplitude A with $kL = 4$, for: (a) $B/L = 1/2$, $\Psi = 0$ rad, (b) $B/L = 1$, $\Psi = 0$ rad, (c) $B/L = 2$, $\Psi = 0$ rad, (d) $B/L = 1/2$, $\Psi = \pi/4$ rad, (e) $B/L = 1$, $\Psi = \pi/4$ rad, and (f) $B/L = 2$, $\Psi = \pi/4$ rad. The plate is shaded black.

to $B = [L/2; L; 2L]$ and $\Psi = (0, \pi/4)$ rad. The axes are normalised with respect to the length L such that the plate (shaded black) occupies the location $|x/L| < 1, |y/B| < 1$. Plots are shown for incident waves of frequency parameter $kL = 4$ propagating in the direction $x \to -\infty$. Figs. 7(a)–7(c) show clear evidence of reflected waves and a shadow zone downwave of the plate. Maximum wave amplitude occurs at the front of the plate and is close to twice the incident wave amplitude, as in the case of a perfectly reflecting wall. This result becomes even more obvious at larger values of B/L as shown in Fig. 7(c). Figs. 7(d)–7(f) show the case of oblique incident waves. We note that the shadow zone rotates with the incident wave direction, whereas maximum wave amplitude occurs adjacent to the longer plate side. Also, in the leading edge region the diffracted waves have amplitude close to unity because of weak wave reflection. Similar results were obtained using the analytical model developed by Porter (2016). Specifically, our Figs. 7(b) and 7(e) coincide with Porter's Fig. 3(a) and (b), again validating the present theoretical model.

4.2. SET 1b and SET 1c: Two rectangular plates

We first consider the case SET 1b which consists of two rectangular plates rigidly connected to one another. We assume $B = L$ and vary the distance between the plates $2l$. The entire platform therefore has dimension $4BL$. Figs. 8(a)–8(b) show the surface plots of C_W as functions of kL and PTO coefficient for two separation distances $l = [L; 2L]$ and $\Psi = 0$ rad. Both cases exhibit several resonant peaks and large bandwidth. The peaks are related to resonance of partially standing water waves in the gap between the rectangular plates, similar to moonpool resonance (Molin, 2001; Zhao et al., 2022), whose frequency can be calculated from the dispersion relation in deep water, i.e., $\omega = \sqrt{n\pi g/(2l)}$, $n = 1, \ldots, \infty$, or equivalently $kL = n\pi L/(2l)$. Furthermore, by comparing Figs. 8(a)–8(b) against the results for the square WEC of area $4BL$ shown in Fig. 5(b), it can be seen that the maximum efficiency value improves although the results depicted in Figs. 8(a)–8(b) are spiky and less regular. Figs. 8(c)–8(d) represent the behaviour of C_W for the same platforms but different incident wave angle $\Psi = \pi/4$ rad. The overall behaviour is similar to Figs. 8(a)–8(b), except for the major peak in Fig. 8(d). The presence of the C_W peaks is explained by analysing the hydrodynamic profiles with kL shown in Fig. 9. The F_h', F_p' and F_r' curves contain peaks at the resonant frequencies seen in C_W, implying that the diffracted wave field governs the overall efficiency. Similarly, the sharp peaks in added mass and radiation damping depicted in Figs. 9(c)–9(d) occur at similar frequencies because of moonpool resonance between the plates. Interestingly, as shown in Fig. 9(b), we note that the maxima/minima for pitch moments coincide with the minima/maxima of roll moments. This is because of the different standing-wave pattern between the plates.

Fig. 10 shows the spatial distribution of the diffracted free surface elevation $|\eta_D|/A$ when $kL = 4$ for $l = [L; 2L]$ and $\Psi = (0, \pi/4)$ rad. Again significant wave reflection occurs at the platform front and a shadow zone exists behind the second plate for $\Psi = 0$ rad. The maximum wave amplitude is about twice the incident wave amplitude, and is hardly affected by increasing distance l. Similarly, the shadow zone is unaltered by the choice of l. Between the plates where $|x| < (l + L)$, a quasi-standing wave pattern occurs in $|\eta_D|$ with three peaks for $l = L$ (see Fig. 10(a)) and five peaks for $l = 2L$ (see Fig. 10(b)). However, the amplitude of these standing waves is always smaller than those localised at the platform front area because of the shadow effect from the first plate. A

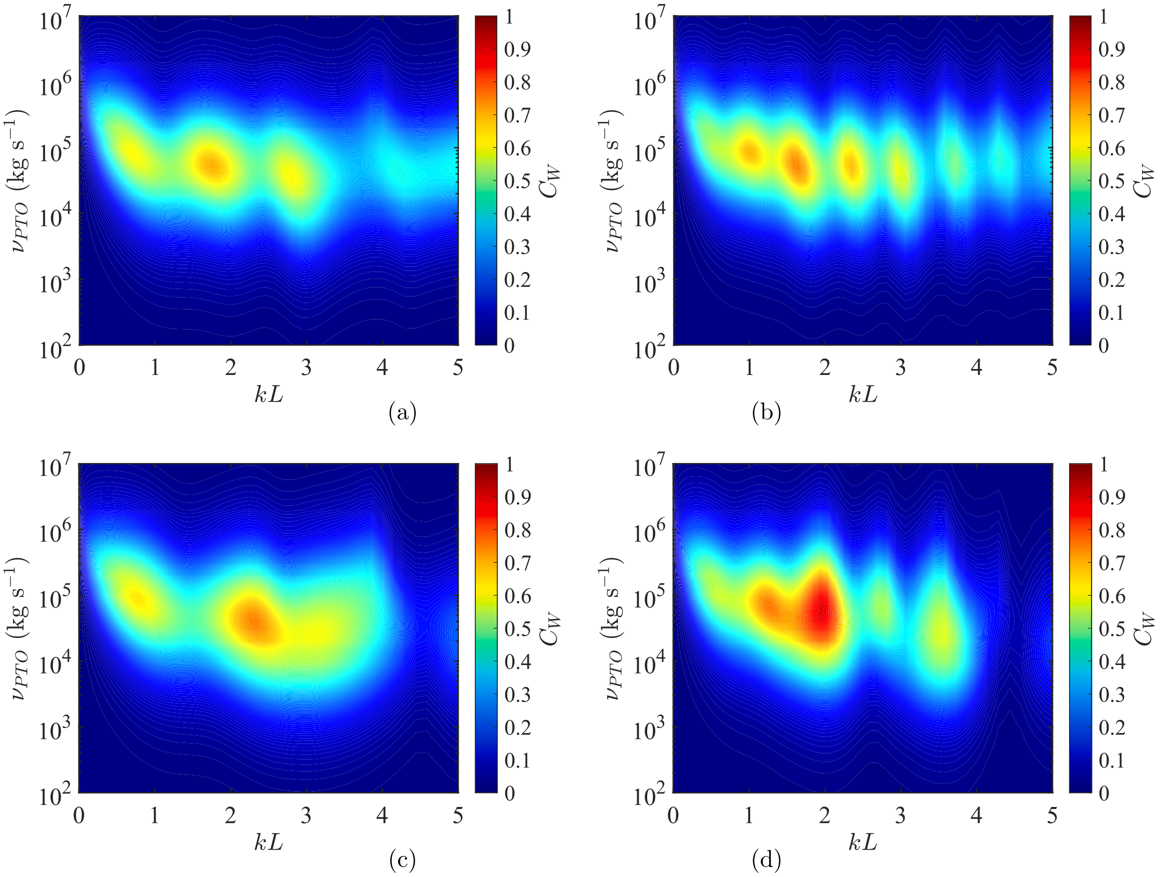

(a) (b) (c) (d)

Fig. 8. Capture-width ratio C_W as a function of kL and PTO coefficient ν_{PTO} for a two-plate platform (SET 1b). Plate width is $B = L$: (a) $l = L$, $\Psi = 0$ rad, (b) $l = 2L$, $\Psi = 0$ rad, (c) $l = L$, $\Psi = \pi/4$ rad, and (d) $l = 2L$, $\Psi = \pi/4$ rad. In the case of incident waves propagating along x, peaks are close to resonant frequencies $kL = n\pi L/(2l), n = 1, \ldots, \infty$.

significantly different pattern occurs for oblique waves as depicted in Figs. 10(c)–10(d). The plate on the upwave side experiences diffracted wave amplitude similar to that in Fig. 7(e), whereas between the plates a strong diffracted wave amplitude occurs as oblique waves penetrate this region which are capable of triggering resonant patterns. This is obvious in Fig. 10(c), whereas for wider distance l this phenomenon diminishes.

Let us now consider the configuration SET 1c, i.e. a platform made of two plates of width $B = L$, rigidly connected to one another and separated by horizontal distance $2b$. Fig. 11(a) depicts the behaviour of C_W with kL and PTO coefficient for the case $b = L$, and Fig. 11(b) shows the behaviour of C_W for larger separation distance $b = 2L$. The platform attains great efficiency in the range $kL = 1 - 2$ and $\nu_{PTO} = 10^4 - 10^6$ kg s^{-1}, especially when compared with the square plate case in Fig. 5(b). This means that maintaining the same wetted area $4BL$ while changing orientation of the two-plate system, it is possible to increase the power extraction efficiency because of constructive interactions between the plates. Furthermore we note the presence of minor peaks at $kL > 2$. As previously depicted in Fig. 6, these peaks correspond to the resonance of standing waves in the gap between the plates. In this case, the waves are symmetrical with respect to the x axis and their frequency is given by $\omega = \sqrt{n\pi g/b}, n = 1, \ldots, \infty$. Note that SET 1c is merely SET 1b rotated by 90 degrees, and so the capture-width ratio for $\Psi = \pi/4$ rad is the same as in Figs. 8(c)–8(d).

Fig. 12 shows the behaviour of hydrodynamic force parameters versus kL. The behaviour in pitch is not as spiky as in heave, or as in Fig. 9. This is because the pitch motion does not generate large waves that propagate along the y axis, thus avoiding standing wave resonances. Hence, the behaviour is similar to that of the single plate analysed in the previous section. Conversely, the heave motion triggers standing wave resonance between the plates, causing the spiky signatures in F_h', μ_{hh}' and λ_{hh}' with kL. By comparing Fig. 12 against Fig. 9 we note that the pitch hydrodynamic force corresponds with the roll hydrodynamic force because this platform is simply equal to platform SET 1b subject to 90 degrees rotation.

Fig. 13 depicts the non-dimensional diffracted wave amplitude for the foregoing pair of parallel plates and fixed non-dimensional wave number $kL = 4$. For plates with relatively small separation distance $b = L$, strong resonant free-surface behaviour occurs in the gap between the plates, as evidenced by the three peaks of amplitude $|\eta_D| \sim 2.5A$ in Fig. 13(a). Downwave of the plates, in the region $x < -L, |y| < L$, the amplitude of the diffracted wave amplitude is close to that of its incident counterpart, i.e., $|\eta_D| \sim A$. This means that incident waves can easily penetrate between the parallel plates and bypass the floating structure almost unaffected.

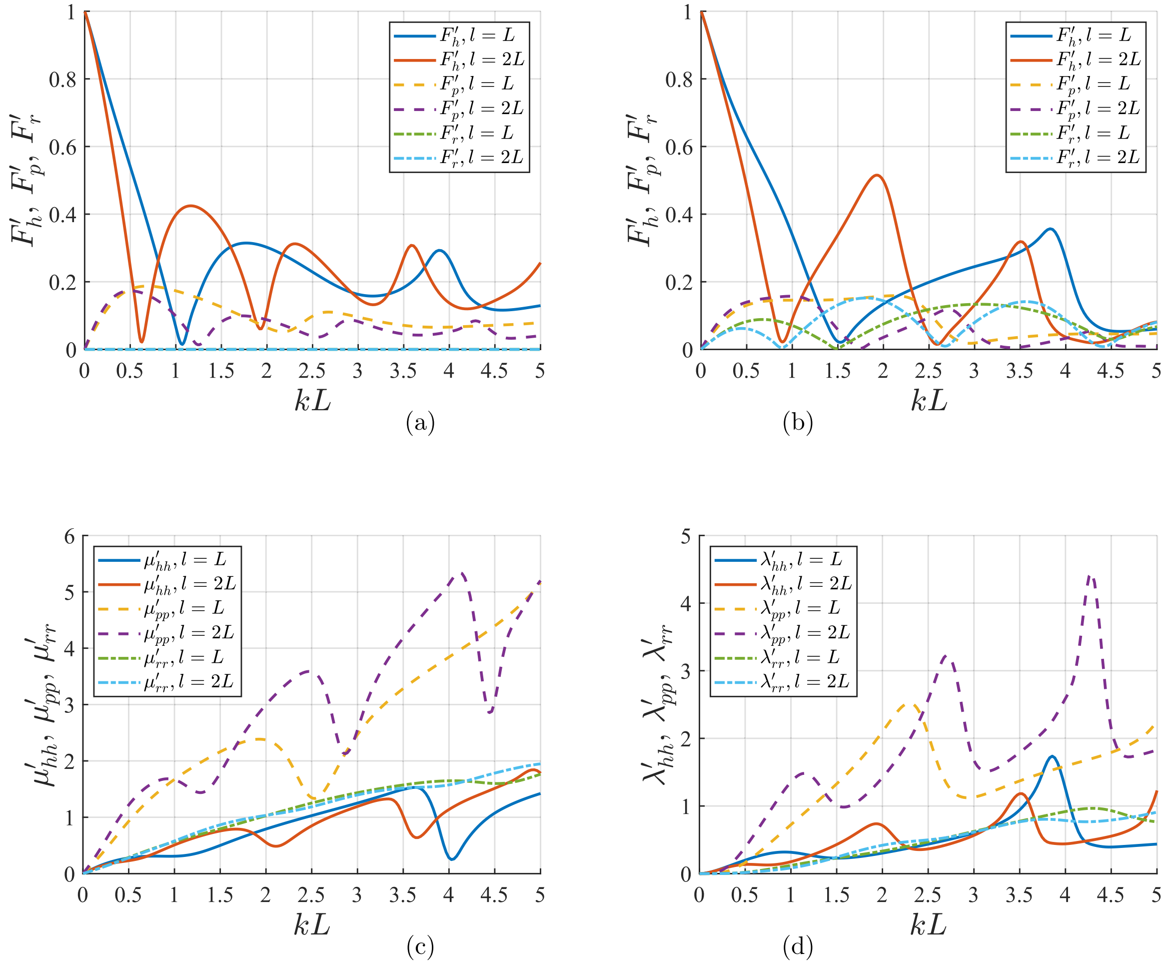

Fig. 9. Hydrodynamic force and moment components with respect to kL for SET 1b with $B = L$ and $l = [L, 2L]$: (a) heave exciting force, pitch and roll exciting moments, $\Psi = 0$ rad; (b) heave exciting force, pitch and roll exciting moments, $\Psi = \pi/4$ rad; (c) heave added mass, pitch and roll added inertia; (d) heave, pitch and roll radiation damping.

Different behaviour occurs when the gap distance b is larger, as shown in Fig. 13(b). In this case five significant peaks occur in the diffracted wave amplitude between the plates and for $x < L$; however the standing wave resonant mechanism seems to have weakened because of the greater b. In front of the platform for $x > L$, a number of wave rays have been generated, the number depending on b and corresponding standing wavelengths. Here, three and five wave rays separated by constant amplitude $|\eta_D| \sim A$ are obtained for $b = [L, 2L]$. A shadow zone has formed behind both plates forming a ~20° angle with the x axis. As before, the diffracted wave patterns for $\Psi = \pi/4$ rad are not presented here because they are the same as those shown in Figs. 10(c)–10(d).

4.3. SET 1d: Four rectangular plates

In this section we investigate SET 1d, consisting of an array of four rectangular plates separated by distances l and b and rigidly connected to each other. For brevity we consider the case when $B = L$, which represents a platform comprising four square plates. Fig. 14(a) displays the C_W behaviour for the same gap distances $b = l = L$. High efficiency is achieved at $kL \sim 1.5$ and a sequence of local maxima for $kL > 2$ driven by resonant standing waves in the gaps between the plates. Here, the frequency bandwidth is large, highlighting the beneficial effect of decomposing the platform into subsystems. Fig. 14(b) presents the corresponding results for wider gap spacing $b = l = 2L$. Although the C_W behaviour is similar to that depicted in Fig. 14(a), it exhibits more peaks due to the increasing number of standing wave modes in the gaps. Figs. 14(c)–14(d) show the case of oblique incident waves $\Psi = \pi/4$ rad for the same platforms. We note that maximum value of efficiency improves because of the large hydrodynamic force in heave; however the peaks tend to narrow as their number reduces causing the overall performance to deteriorate.

Fig. 15 depicts the behaviour of the exciting force, added mass and radiation damping parameters in heave, pitch and roll with non-dimensional wave number. The results are similar to that in Fig. 9 for the two-plate case SET 1b. The main difference is the

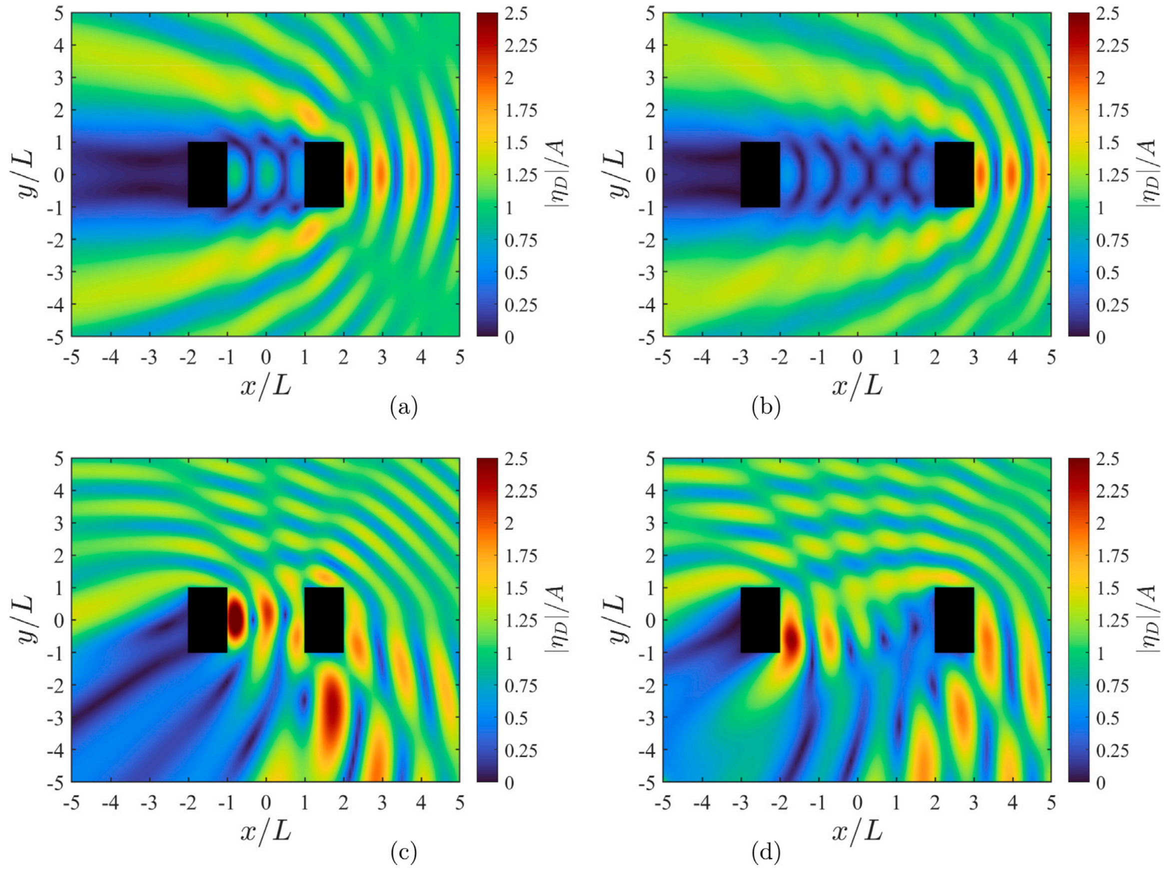

Fig. 10. Contour plots of the spatial distribution of the non-dimensional modulus of diffracted wave elevation for SET 1b. Parameters are $kL = 4$, $B = L$, and: (a) $l = L$, $\Psi = 0$ rad, (b) $l = 2L$, $\Psi = 0$ rad, (c) $l = L$, $\Psi = \pi/4$ rad, and (d) $l = 2L$, $\Psi = \pi/4$ rad. The two-plate platform is shaded black.

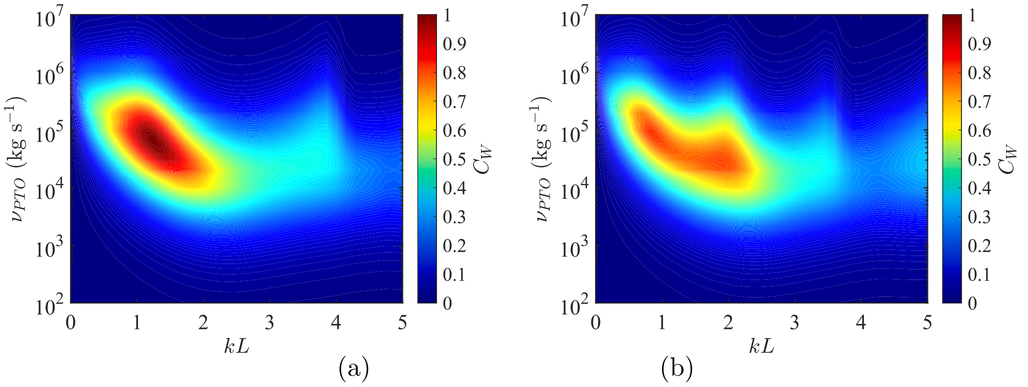

Fig. 11. Capture-width ratio C_W as a function of kL and PTO coefficient ν_{PTO} for a two-plate platform (SET 1c). Plate width is $B = L$. (a) $b = L$ and (b) $b = 2L$. Peaks are close to resonant standing-wave frequencies.

increased number of spikes for μ_{pp} and λ_{pp} in the four-rectangular-plate case, even though the magnitude is essentially the same. This indicates that the overall hydrodynamic properties are primarily influenced by the gap distance $2l$.

Fig. 16 shows the corresponding diffracted wave field. When $\Psi = 0$ rad there is some similarity with the results in Fig. 13. In front of the platform $x > (L + l)$ the behaviour is very similar, in terms of both magnitude and wavy pattern. The standing wave pattern in the gap between the plates at first row $|y| < b$, $x > 0$ is very similar to that presented in Fig. 13. The main differences occur in the region $x < 0$, due to the influence of the second row of plates on the local wave hydrodynamics. The results obtained for

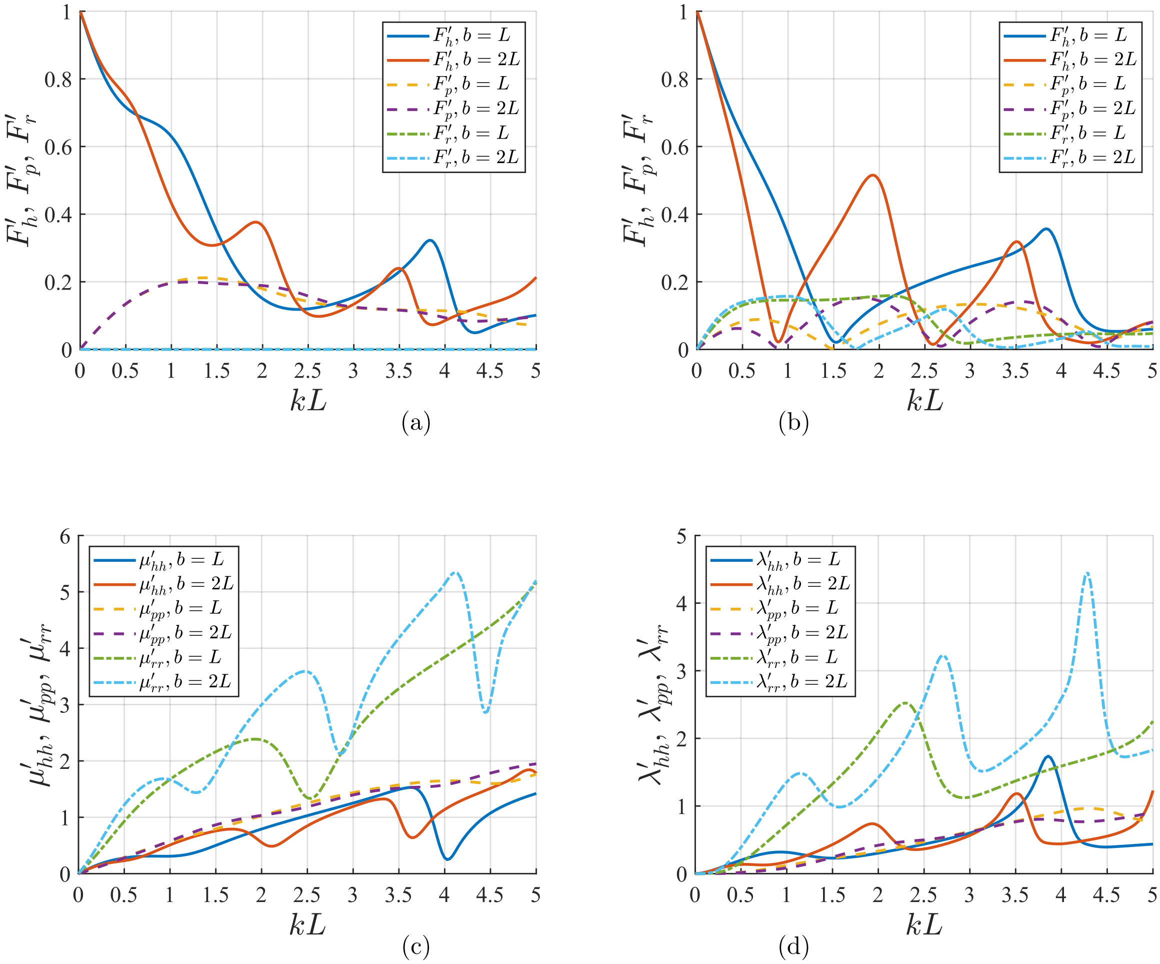

(a) (b)

(c) (d)

Fig. 12. Hydrodynamic force and moment components with respect to kL for SET 1c with $B = L$, and $b = [L, 2L]$: (a) heave exciting force, pitch and roll exciting moments, $\Psi = 0$ rad; (b) heave exciting force, pitch and roll exciting moments, $\Psi = \pi/4$ rad; (c) heave added mass, pitch and roll added inertia; (d) heave, pitch and roll radiation damping.

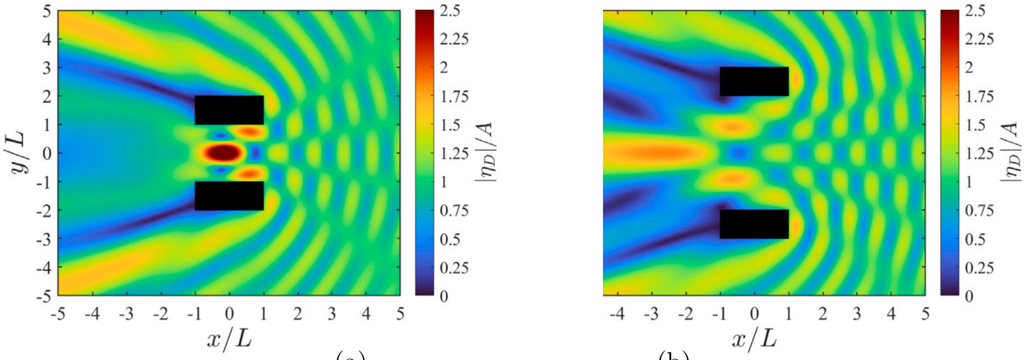

(a) (b)

Fig. 13. Contour plots of the spatial distribution of the non-dimensional modulus of diffracted wave elevation for SET 1c. Parameters are $kL = 4$, $B = L$, and : (a) $b = L$, and (b) $b = 2L$. The two-plate platform is shaded black.

oblique waves and distance $b = l = B$ shown in Fig. 16(c) are characterised by strong standing wave interaction and the existence of oblique wave rays. We also note the presence of a wide shadow zone in the downwave side. For wider plate distance we obtain the wave pattern in Fig. 16(d) and note a shadow zone between the plates. This is significantly different from the previous case;

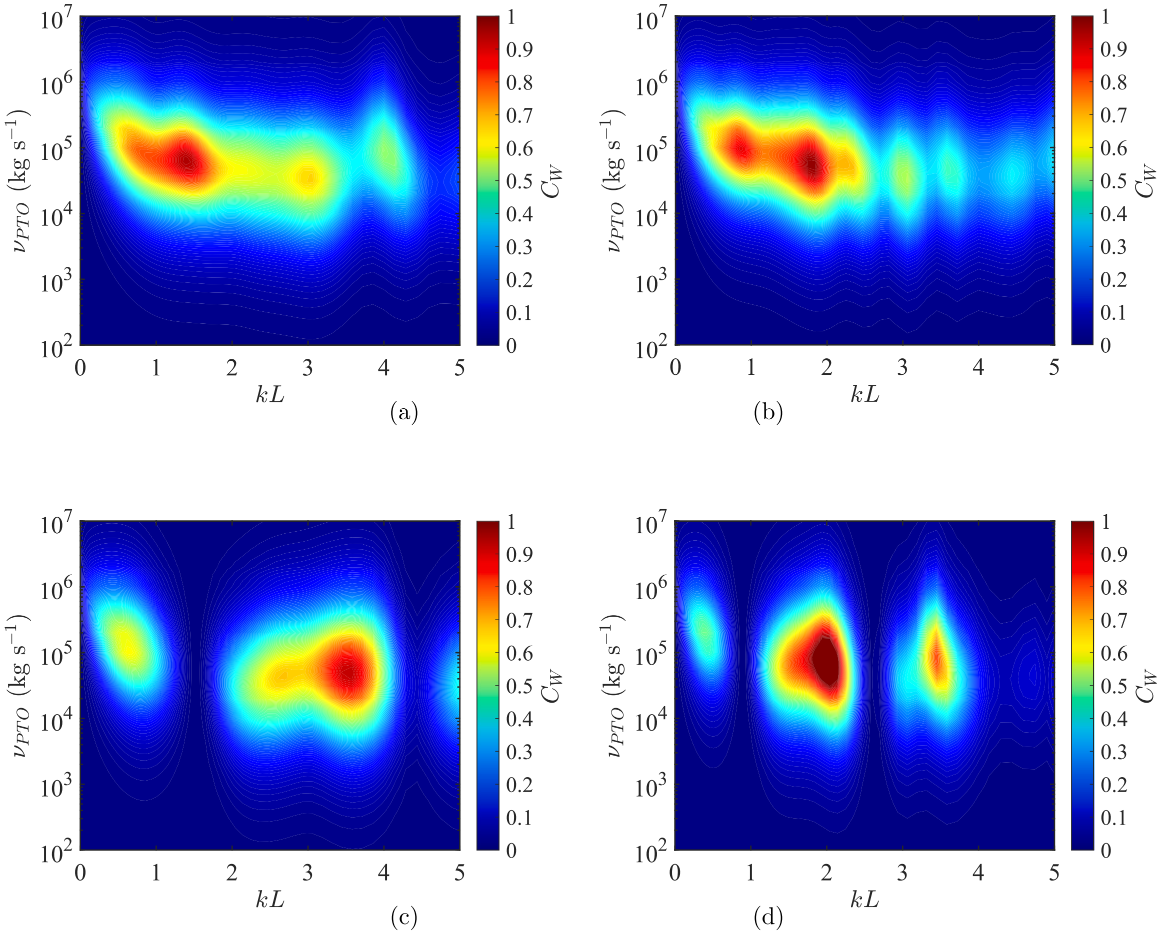

(a) (b) (c) (d)

Fig. 14. Capture-width ratio C_W as a function of kL and PTO coefficient ν_{PTO} for a four-plate platform (SET 1d). Plate parameters are $B = L$: (a) $b = l = L$, $\Psi = 0$ rad, (b) $b = l = 2L$, $\Psi = 0$ rad, (c) $b = l = L$, $\Psi = \pi/4$ rad, and (d) $b = l = 2L$, $\Psi = \pi/4$ rad.

hence the parameters b and l play a significant role because they can induce resonance at certain incident wave frequencies. This is crucial for structural purposes because large waves correspond to high amplitude forces.

4.4. SET 2: T-shaped and cross-shaped platform

We now analyse the behaviour of a T-shaped and cross-shaped platform described by SET 2 (see Fig. 1). To make comparisons against the cases analysed in the previous section we set the plate width $B = L$ and indentation width $l = b = L/2$. Fig. 17 shows the capture width ratio C_W as a function of non-dimensional wave number and PTO coefficient for the foregoing cases. Figs. 17(a)–17(c) refer to $\Psi = 0$ rad, whereas Figs. 17(d)–17(f) depict the case of oblique incident waves where $\Psi = \pi/4$ rad. We note that for $\Psi = 0$ rad, by translating the indentation at the platform front we can increase the efficiency bandwidth up to great frequencies. This configuration corresponds to the case SET 2c as shown in Fig. 17(c). The opposite occurs in the case of oblique waves, where SET 2a is the most efficient configuration. At low frequency there is no significant difference in terms of efficiency, and all the cases behave in the same way for assigned Ψ. This is because the plate edge in $x = L$ acts as a barrier that strongly deflects water waves of small wavelength in $|y| > B$. Conversely, long waves are unaffected by the size of platform indentation, and the power extraction efficiency is unchanged.

Fig. 18 illustrates the corresponding dependence of exciting force, added-mass, and radiation damping in heave and pitch on the non-dimensional wave number. Figs. 18(a)–18(b) show that for $kL < 2$ we obtain the same value of heave force F_h', because of the large incident wavelength and small influence of plate indentations. The pitch exciting force F_p' tends to a non-zero value for small kL because of non-symmetry of the platform geometry for SET 2a and SET 2c. In other words, the static equilibrium position of the platform does not coincide with the horizontal plane $z = 0$. We also note that for $\Psi = 0$ rad, the heave force results are larger for SET 2c, whereas for oblique waves, F_h' is maximised for SET 2a. This explains the dependence of C_W on incident wave direction shown in Fig. 17. The behaviour of the added mass and radiation damping appears to be similar for all configurations, and is exactly the same for the T-shaped platforms because of symmetry of radiated wave field, whereas for SET 2b, λ_{pp} and μ_{pp}

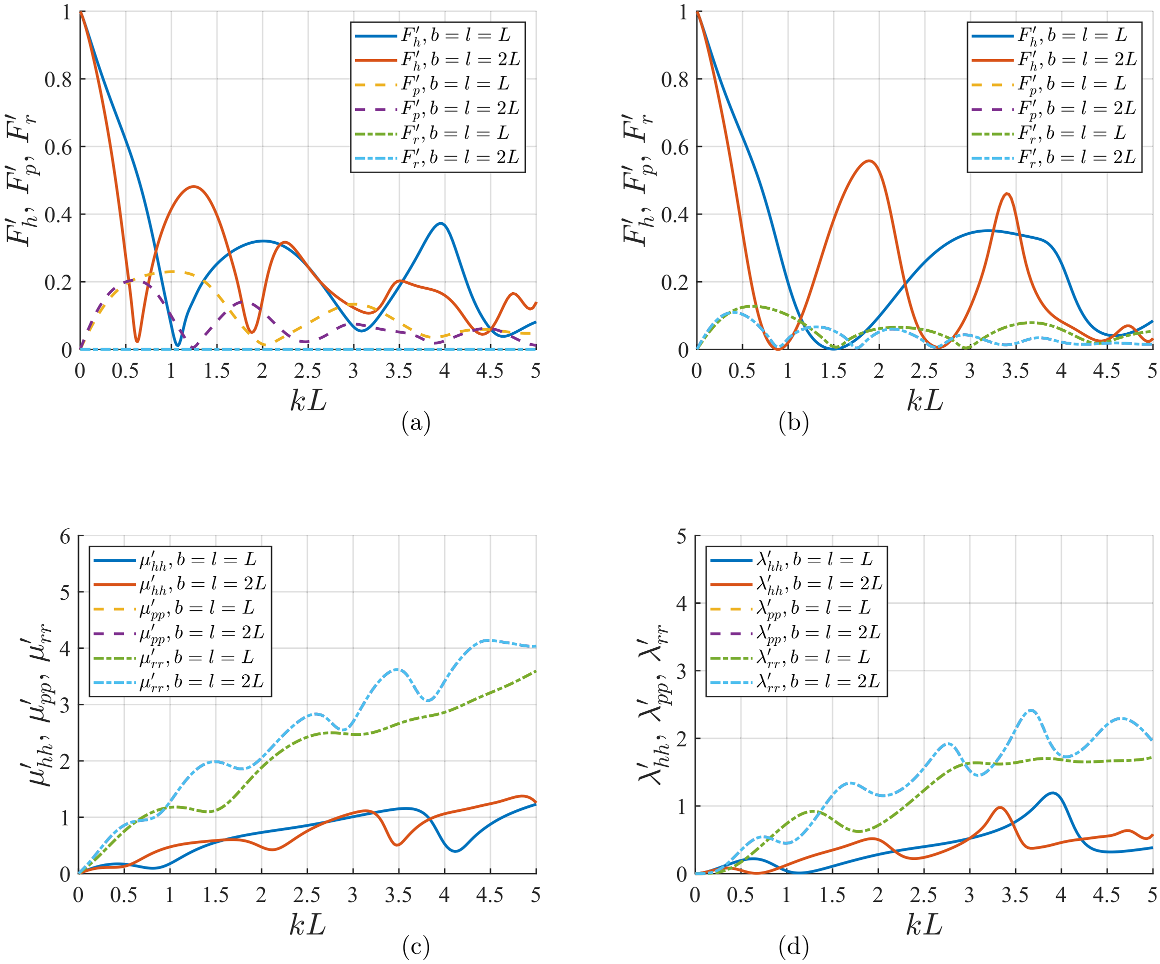

(a) (b)

(c) (d)

Fig. 15. Hydrodynamic force and moment components with respect to kL for SET 1d with $B = L$, and $b = l = [L, 2L]$: (a) heave exciting force, pitch and roll exciting moments, $\Psi = 0$ rad; (b) heave exciting force, pitch and roll exciting moments, $\Psi = \pi/4$ rad; (c) heave added mass, pitch and roll added inertia; (d) heave, pitch and roll radiation damping.

coincide with λ_{rr} and μ_{rr}, again, because of symmetry of platform geometry and consequent radiated waves pattern. It should be noted that all the plots are very similar to those obtained for the single square plate in Fig. 6, especially at small frequencies. This again implies similar capture-width ratio values, as found earlier in this section.

We now turn to the diffracted wave field depicted in Fig. 19 for $kL = 4$. At the downwave side, independently of incident wave direction, the behaviour of $|\eta_D|$ is very similar in all cases. Conversely, in the region close to the plate front we observe some important differences due to the indentation position. We remark that we are assuming $kL = 4$, i.e., the wavelength is comparable to the platform size, implying that incident waves may interact strongly with the indentation geometry. Specifically, Fig. 19(a) shows the presence of a single wave ray of amplitude $|\eta_D|/A \sim 1.6$ in the region $x > L$. Surprisingly, the cross-shaped platform case of Fig. 19(b) does not scatter significant energy in the region $y = 0, x > L$ but instead large-amplitude waves propagate at $\sim 45°$. Conversely, the behaviour of diffracted waves in the case of the T-shaped platform depicted in Fig. 19(c) resembles that depicted previously in Fig. 7(b) for a single square plate. For $\Psi = \pi/4$ rad and SET 2a, we obtain the wave pattern shown in Fig. 19(a). Interestingly, a large diffracted wave amplitude $|\eta_D|/A \sim 2.5$ occurs close to the platform corner exposed to incoming waves. The cross-shaped platform exhibits similar behaviour, with the region at the plate front in Fig. 19(f) having some similarity with the upwave side depicted in Fig. 7(e).

4.5. SET 3: C-shaped and I-shaped platforms

We now investigate the behaviour of platforms belonging to the configurations SET 3. For comparison against previous cases, we fix the base width to be $B = L$ and indentation lengths $b = l = L/2$, and consider $\Psi = (0, \pi/4)$ rad.

Fig. 20(a) presents contours of the capture-width ratio in the kL-PTO coefficient space for the case SET 3a. High efficiency is achieved at $kL \sim 2$ and significant bandwidth. Peak capture-width ratio is $C_W \sim 0.7$, comparable with value obtained for the

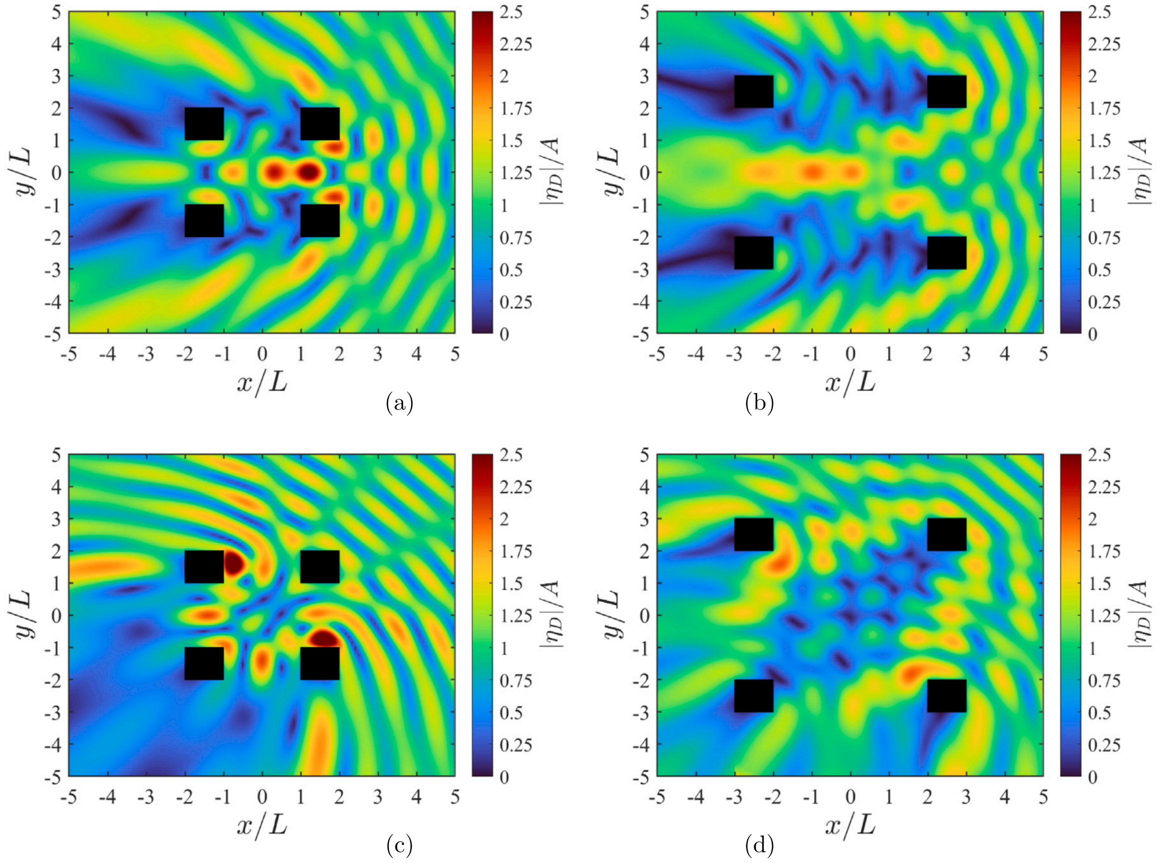

Fig. 16. Contour plots of the non-dimensional modulus of diffracted wave elevation for SET 1d. Parameters are $kL = 4$, $B = L$ and: (a) $B = b = l$, $\Psi = 0$ rad, (b) $B = b/2 = l/2$, $\Psi = 0$ rad, (c) $B = b = l$, $\Psi = \pi/4$ rad, and (d) $B = b/2 = l/2$, $\Psi = \pi/4$ rad. The four-plate platform is shaded black.

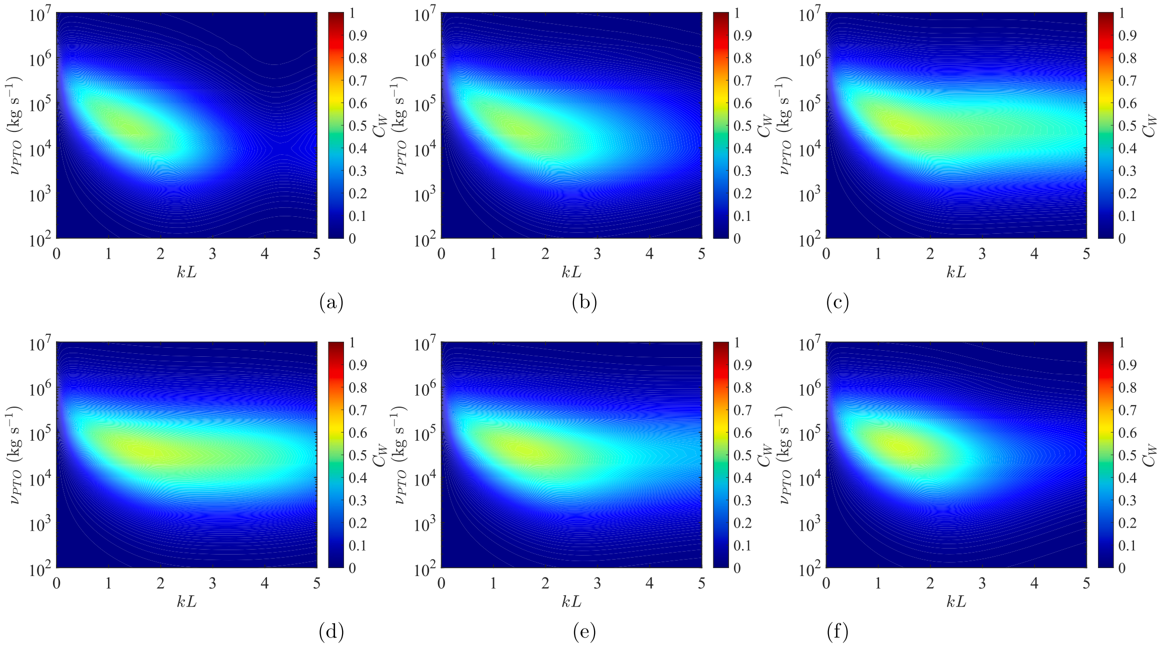

Fig. 17. Capture-width ratio C_W as a function of angle of incidence Ψ, kL and PTO coefficient ν_{PTO} for $B = L$, $b = l = L/2$ and configurations: (a) SET 2a, $\Psi = 0$ rad, (b) SET 2b, $\Psi = 0$ rad, (c) SET 2c, $\Psi = 0$ rad, (d) SET 2a, $\Psi = \pi/4$ rad, (e) SET 2b, $\Psi = \pi/4$ rad, (f) SET 2c, $\Psi = \pi/4$ rad.

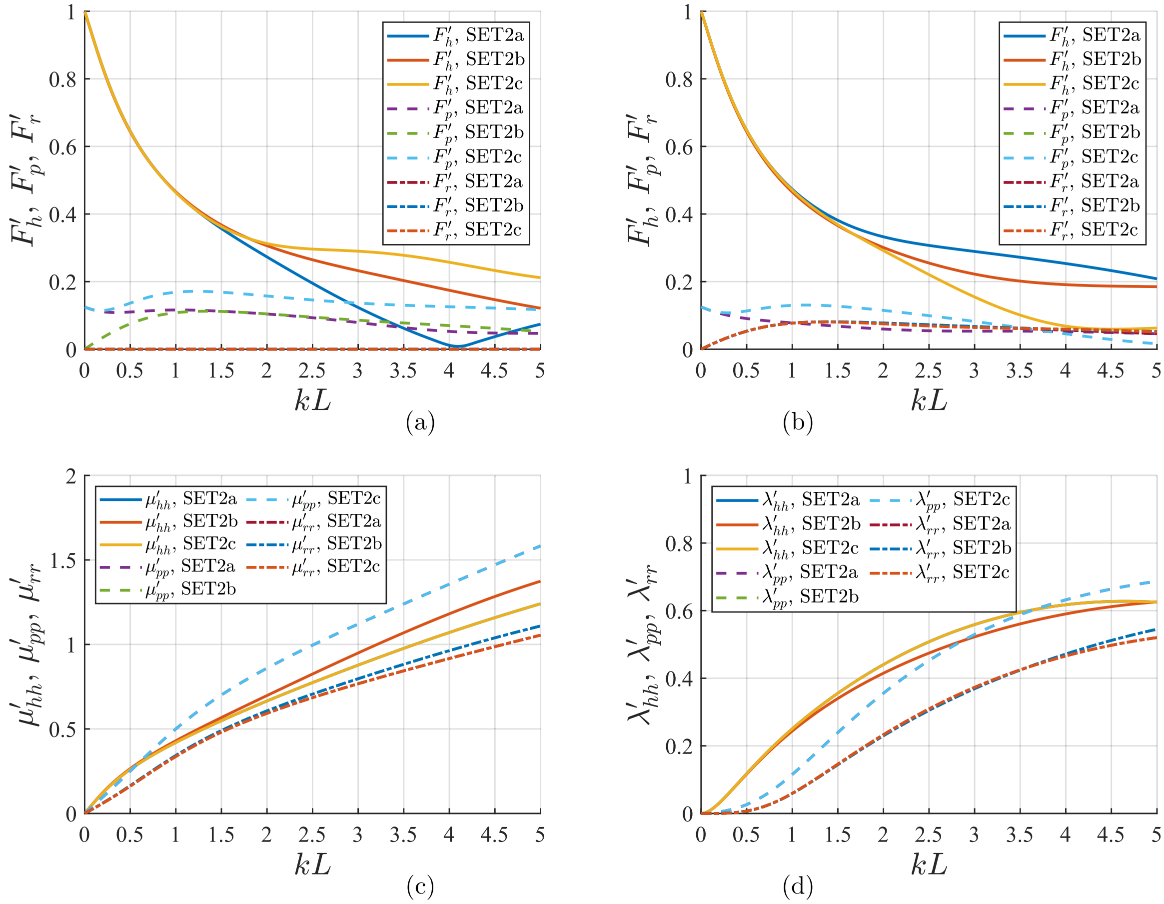

(a) (b)

(c) (d)

Fig. 18. Hydrodynamic force and moment components with respect to kL for SET 2 with $B = L$, and $b = l = L/2$: (a) heave exciting force, pitch and roll exciting moments, $\Psi = 0$ rad; (b) heave exciting force, pitch and roll exciting moments, $\Psi = \pi/4$ rad; (c) heave added mass, pitch and roll added inertia; (d) heave, pitch and roll radiation damping.

square case in Fig. 5(b). It should be noted however that although this C-shaped platform has smaller wetted area, we are able to attain similar power extraction by reducing the platform size and mitigating the consequent economic impact, which is crucial for optimising the design of such WECs. Figs. 20(b)–20(c) show the results obtained for an I-shaped symmetric platform (SET 3b) and a C-shaped platform (SET 3c) with indentation localised at the plate downwave side. In these cases the power extraction efficiency tends to decrease, even though the bandwidth improves. A similar trend is shown in Fig. 17 for different T-shaped platforms. Figs. 20(d)–20(f) represent the capture-width ratio for the same configurations but $\Psi = \pi/4$ rad. We note that the overall efficiency is the same in each case except SET 3a at very large frequencies.

Fig. 21 shows the hydrodynamic force parameters as a function of the dimensionless wave number kL. At low values of kL the behaviour of the force parameters is similar to that in Fig. 18; however, appreciable differences appear at large kL. Moreover, we note that the C-shaped platforms (SET 3a and SET 3c) possess the same added mass and radiation damping which are independent of platform orientation with respect to the incident wave field. Therefore differences in power extraction efficiency are primarily due to differences in the exciting forces.

Finally, Fig. 22 presents the spatial distribution of the diffracted wave amplitude. Note that when the indentation is located at the upwave side (see Figs. 22(a)–22(d)) and at the middle (see Figs. 22(b)–22(e)), it is possible to focus waves at the platform front. Here, maximum of the diffracted wave amplitude can be $|\eta_D|/A \sim 2.5$, larger than in all the previous cases except for the two-plate and four-plate configurations in figs. 13(a)–16(a). The shadow zone behind the platform remains similarly unchanged, and rotates with the incident wave direction, confirming that the indentation position does not affect the diffracted wave field in the downwave region.

5. Conclusions

This paper describes a theoretical model of the wave-response behaviour of a platform composed of rectangular rigid plates connected to a PTO cable system. The mathematical model is based on linearised potential-flow theory, whereby the method of

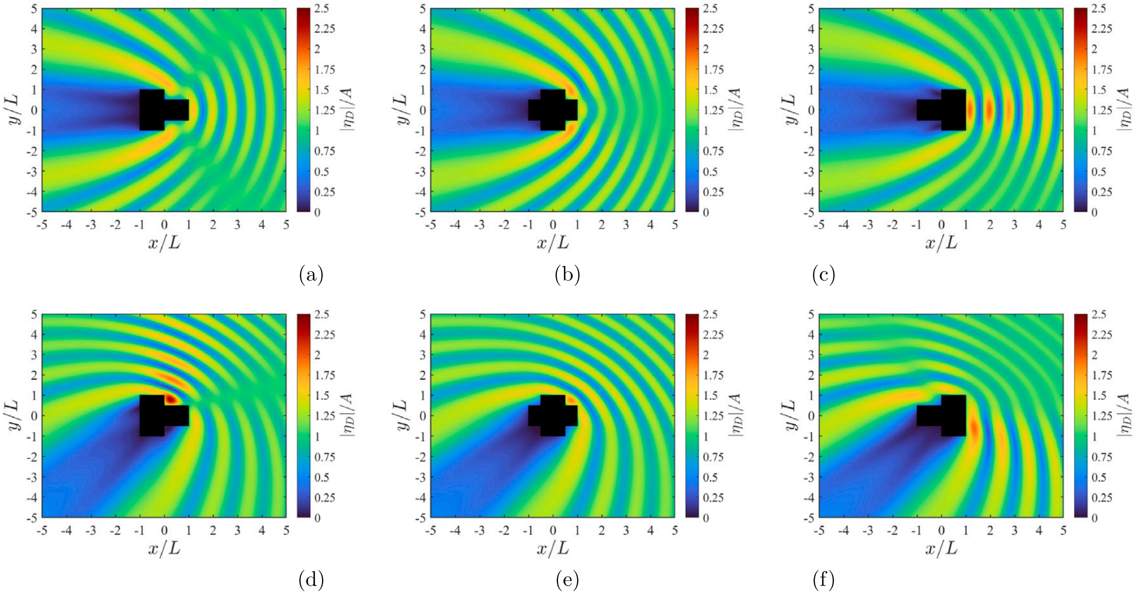

(a) (b) (c)

(d) (e) (f)

Fig. 19. Contour plots of the non-dimensional modulus of diffracted wave elevation for $kL = 4$, $B = L$, $b = l = L/2$ and configurations: (a) SET 2a, $\Psi = 0$ rad, (b) SET 2b, $\Psi = 0$ rad, (c) SET 2c, $\Psi = 0$ rad, (d) $B/L = 2$, $\Psi = \pi/4$ rad, (e) $B/L = 2$, $\Psi = \pi/4$ rad, and (f) $B/L = 2$, $\Psi = \pi/4$ rad. The platform is shaded black.

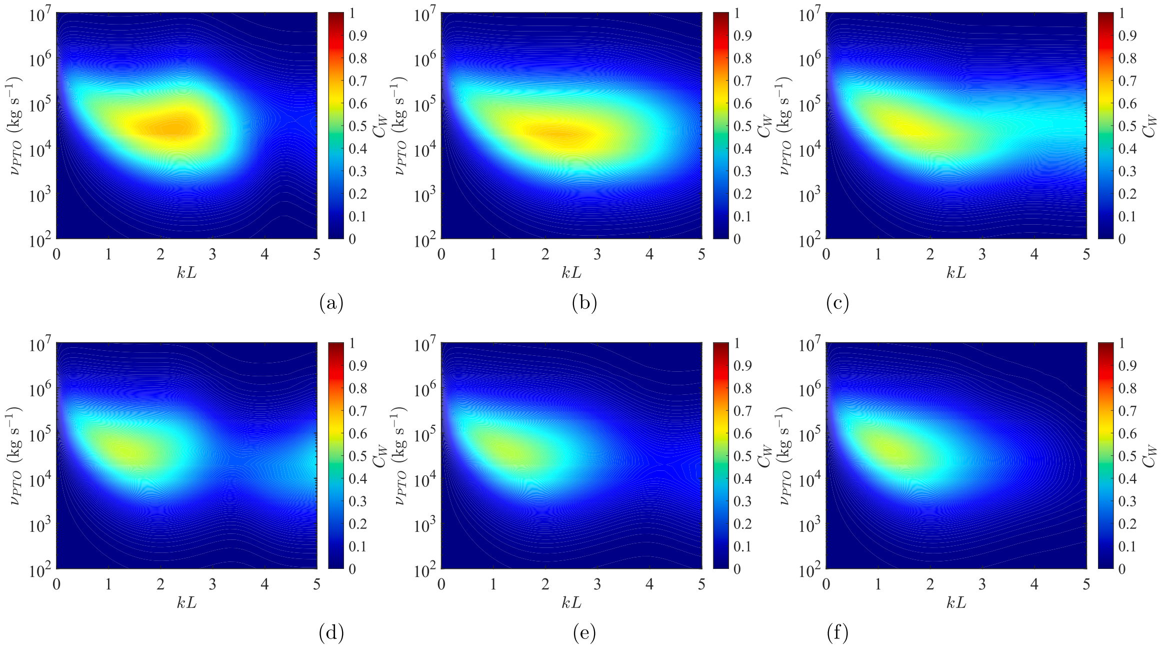

(a) (b) (c)

(d) (e) (f)

Fig. 20. Capture-width ratio C_W as a function of angle of incidence Ψ, kL and PTO coefficient ν_{PTO} for $B = L$, $b = l = L/2$ and configurations: (a) SET 3a, $\Psi = 0$ rad, (b) SET 3b, $\Psi = 0$ rad, (c) SET 3c, $\Psi = 0$ rad, (d) SET 3a, $\Psi = \pi/4$ rad, (e) SET 3b, $\Psi = \pi/4$ rad, (f) SET 3c, $\Psi = \pi/4$ rad.

dry modes is combined with Green's function and Green's theorem to solve for the hydrodynamic radiation and diffraction velocity potentials.

Experimental data on the response of a rigid floating plate in regular waves were obtained from physical tests conducted in the COAST laboratory at the University of Plymouth. The effect of heave and pitch modes on overall plate motion was elucidated over a wide range of fundamental wave frequencies. Very close agreement was obtained between the experimental and analytical response spectra. Using Fourier analysis the second harmonics of the plate response were determined from the measured displacement time series. The results revealed second-harmonic peaks of significant amplitude. In practice, these second-order response spikes would

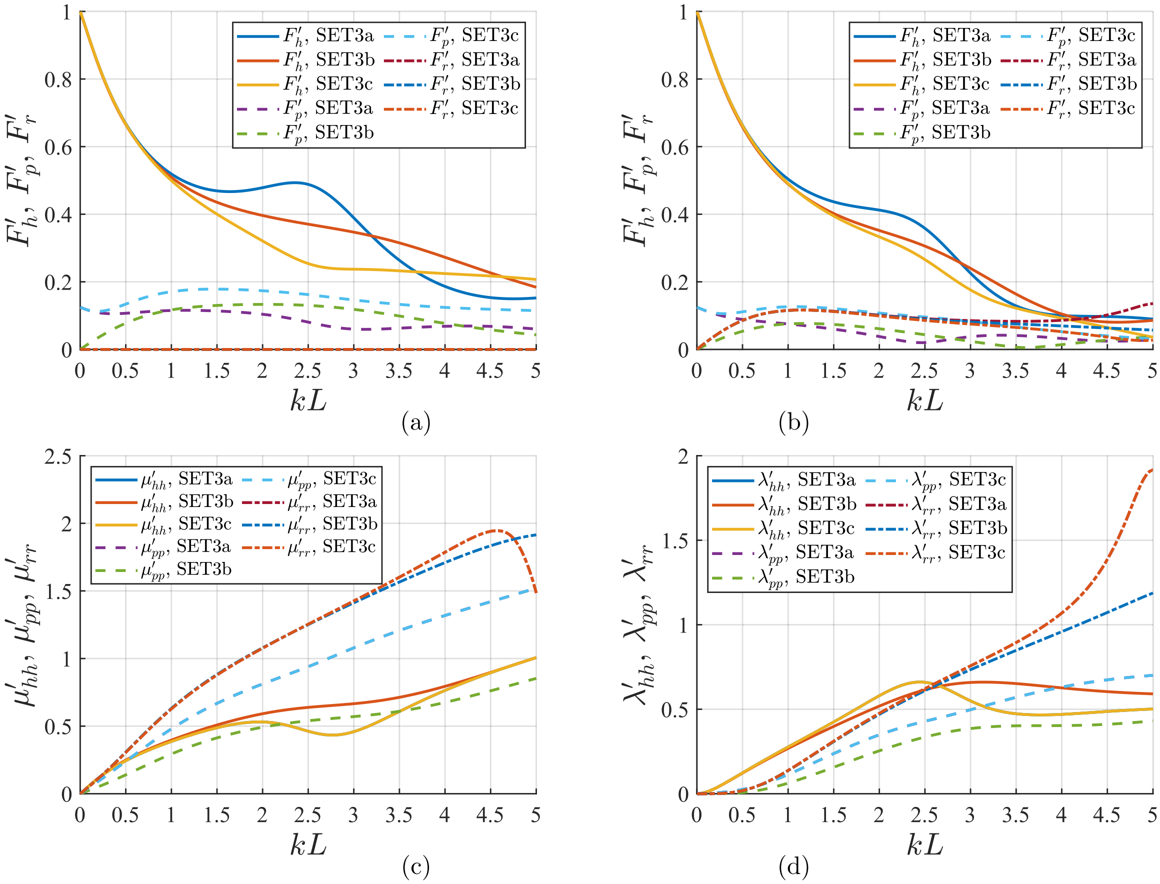

(a) (b) (c) (d)

Fig. 21. Hydrodynamic force and moment components with respect to kL for SET 3 with $B = L$, and $b = l = L/2$: (a) heave exciting force, pitch and roll exciting moments, $\Psi = 0$ rad; (b) heave exciting force, pitch and roll exciting moments, $\Psi = \pi/4$ rad; (c) heave added mass, pitch and roll added inertia; (d) heave, pitch and roll radiation damping.

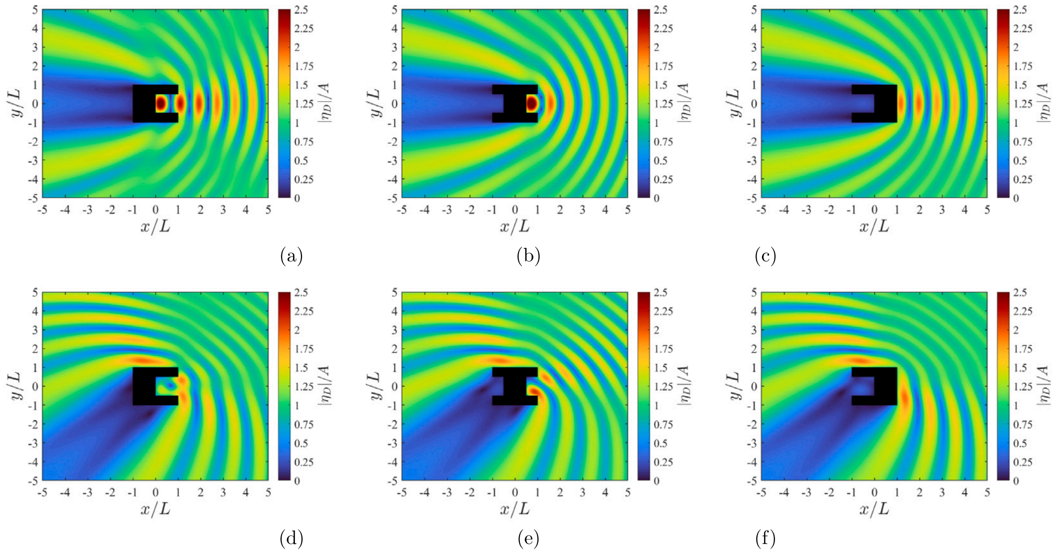

(a) (b) (c)

(d) (e) (f)

Fig. 22. Contour plots of the non-dimensional modulus of diffracted wave elevation for $kL = 4$, $B = L$, $b = l = L/2$ and configurations: (a) SET 3a, $\Psi = 0$ rad, (b) SET 3b, $\Psi = 0$ rad, (c) SET 3c, $\Psi = 0$ rad, (d) SET 3a, $\Psi = \pi/4$ rad, (e) SET 3b, $\Psi = \pi/4$ rad, and (f) SET 3c, $\Psi = \pi/4$ rad. The platform is shaded black.

cause additional external forces on the mooring lines and greater structural stress. The results support the use of potential flow theory developed herein as a tool to predict body motion in ocean waves.

The wave power extraction efficiency was assessed for generalised incident wave direction and several platform configurations, including single and arrays of rectangular plates, and complex C-, I-, cross- and T-shaped platforms. The analytical model indicated that single rectangular slender plates are potentially capable of absorbing significant energy, at the cost of decreased bandwidth. For arrays of rectangular plates it was found that the effect of increasing distance between the plates is to increase the number of moonpool resonant frequencies and capture-width ratio bandwidth. The C-shaped platforms exhibited high energy extraction efficiency, and are capable of absorbing the same wave power as rectangular plates of the same width while having the considerable benefit of smaller wetted area. This indicates the potential use of the present theoretical model by design engineers to alter WEC platform geometry to maximise the capture-width ratio while reducing their cost.

The theoretical model presented herein can be extended to any configuration or shape, but is limited to rigid floating objects of small draft and PTO cables characterised by linear damping. We recommend that analysis of the optimal distribution of both PTO devices and platform elasticity be undertaken, supplemented by further physical tests. Such studies would lead to the improved design of plate WEC devices in ocean waves, and would help the development of modern technologies such as floating offshore solar energy farms.

Funding

S. Michele, J. Guichard and D. Greaves acknowledge support from R&D Solutions Fund by Enterprise Solutions from the University of Plymouth, Supergen ORE Hub and EPSRC project EP/W003732/1.

CRediT authorship contribution statement

S. Michele: Writing – review & editing, Writing – original draft, Visualization, Validation, Supervision, Software, Resources, Project administration, Methodology, Investigation, Funding acquisition, Formal analysis, Data curation, Conceptualization. **S. Zheng:** Writing – review & editing, Writing – original draft, Visualization, Methodology. **E. Renzi:** Writing – review & editing, Writing – original draft, Visualization. **J. Guichard:** Writing – review & editing, Writing – original draft, Validation, Project administration, Funding acquisition, Conceptualization. **A.G.L. Borthwick:** Writing – review & editing, Writing – original draft, Visualization, Supervision. **D.M. Greaves:** Writing – review & editing, Writing – original draft, Visualization, Supervision, Project administration, Funding acquisition.

Declaration of competing interest

The authors declare that they have no known competing financial interests or personal relationships that could have appeared to influence the work reported in this paper.

Data availability

Data will be made available on request.

Acknowledgements

We would like to express our deep gratitude to one of the anonymous reviewers who recommended a simplification to the Green's function. This was adopted in the paper. All authors approved the version of the manuscript to be published.

Appendix. Convergence of panel method

In this section we analyse the convergence of the panel method by analysing the behaviour of heave ζ_h, pitch ζ_p and roll ζ_h responses, versus kL for various panel numbers N_p. For brevity, we consider the free-response of the configuration SET 1a for $B = 2L$ and angle of incidence $\Psi = \pi/4$ rad. Fig. A.23 shows that for $N_p = 900$ we reach good convergence. We should point out that other authors such as Meylan (2002), indicate that 900 panels are sufficient, whereas Newman (1985) suggests that "a large number of discrete "panel" elements must be utilised, typically between 100 and 1000". For these reasons, in the calculations presented in this paper, we decide to use $N_p = 1000$.

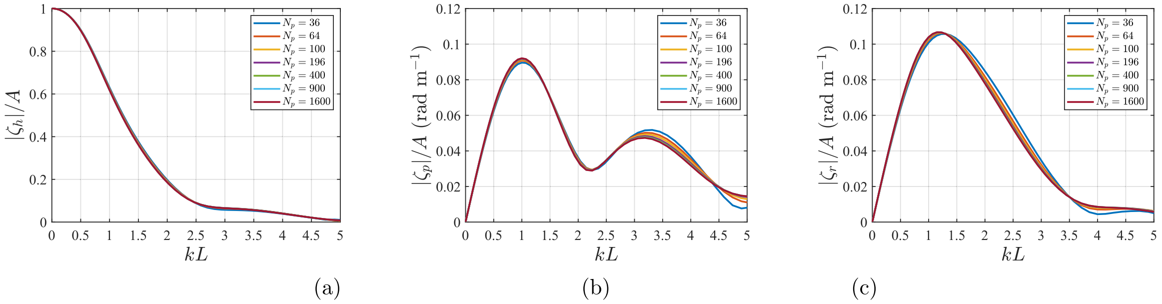

Fig. A.23. Behaviour of normalised heave, pitch and roll free-response versus kL for various numbers of panels N_p. The plate belongs to SET 1a, whereas $B = 2L$ and angle of incidence is set $\Psi = \pi/4$ rad.

References

Bennetts, L.G., Biggs, N.R.T., Porter, D., 2007. A multi-mode approximation to wave scattering by ice sheets of varying thickness. J. Fluid Mech. 579, 413–443.

Bennetts, L.G., Peter, M.A., Squire, V.A., Meylan, M.H., 2010. A three-dimensional model of wave attenuation in the marginal ice zone. J. Geophys. Res. Oceans 115 (C12).

Farina, L., Martin, P.A., 1998. Scattering of water waves by a submerged disc using a hypersingular integral equation. Appl. Ocean Res. 20, 121–134.

Geng, T., Liu, H., Wang, Q., Dias, F., 2022. Wave scattering by a three-dimensional submerged horizontal rectangular plate in a channel: experiments and numerical computations. J. Fluid Mech. 935, A23.

Gradshteyn, I.S., Ryzhik, I.M., 2007. Table of Integrals, Series, and Products, seventh ed. Academic Press, New York.

Kabakhpasheva, T., Korobkin, A.A., 2002. Hydroelastic behaviour of compound floating plate in waves. J. Engrg. Math. 44, 21–44.

Kohout, A., Meylan, M., Sakai, S., Hanai, K., Leman, P., Brossard, D., 2007. Linear water wave propagation through multiple floating elastic plates of variable properties. J. Fluids Struct. 23, 649–663.

Korobkin, A., Khabakhpasheva, T., Shishmarev, K., 2023. Eigenmodes and added-mass matrices of hydroelastic vibrations of complex structures. J. Fluid Mech. 970, A14.

Liang, H., Zheng, S., Magee, A., Greaves, D., 2022. Water wave interactions with perforated elastic disks: Quadratic pressure discharge condition. Phys. Rev. Fluids 7, 054802.

Liang, H., Zheng, S., Shao, Y., Chua, K.H., Choo, Y.S., Greaves, D., 2021. Water wave scattering by impermeable and perforated plates. Phys. Fluids 33, 077111.

Linton, C.M., McIver, P., 2001. Mathematical Techniques for Wave/Structure Interactions. London, UK, Chapman & Hall/CRC.

Martin, P.A., Farina, L., 1997. Radiation of water waves by a heaving submerged horizontal disc. J. Fluid. Mech. 337, 365–379.

Mei, C.C., 1997. Mathematical Analysis in Engineering. Cambridge University Press, New York.

Mei, C.C., Stiassnie, M., Yue, D.K.-P., 2005. Theory and Application of Ocean Surface Waves. World Scientific, Singapore.

Meylan, M.H., 2002. Wave response of an ice floe of arbitrary geometry. J. Geophys. Res. 107, C1.

Meylan, M.H., Ilyas, M., Lamichhane, B.P., Bennetts, L.G., 2021. Swell-induced flexural vibrations of a thickening ice shelf over a shoaling seabed. R. Soc. Lond. A 477, 20210173.

Meylan, M.H., Squire, V.A., 1996. Response of a circular ice floe to ocean waves. J. Geophys. Res. 101 (C4), 8869–8884.

Michele, S., Buriani, F., Renzi, E., van Rooij, M., Jayawardhana, B., Vakis, A., 2020. Wave energy extraction by flexible floaters. Energies 13, 6167.

Michele, S., Sammarco, P., d'Errico, M., 2016a. The optimal design of a flap gate array in front of a straight vertical wall: resonance of the natural modes and enhancement of the exciting torque. Ocean Eng. 118, 152–164.

Michele, S., Sammarco, P., d'Errico, M., 2016b. Theory of the synchronous motion of an array of floating flap gates oscillating wave surge converter. Proc. R. Soc. A 472, 20160174.

Michele, S., Zheng, S., Buriani, F., Borthwick, A.G.L., Greaves, D.M., 2023. Floating hydroelastic circular plate in regular and irregular waves. Eur. J. Mech. B Fluids 99, 148–162.

Michele, S., Zheng, S., Greaves, D.M., 2022. Wave energy extraction from a floating flexible circular plate. Ocean Eng. 245, 110275.

Michele, S., Zheng, S., Renzi, E., Borthwick, A.G.L., Greaves, D.M., 2024. Hydroelastic theory for offshore floating plates of variable flexural rigidity. J. Fluids Struct. 125, 104060.

Molin, B., 2001. On the piston and sloshing modes in moonpools. J. Fluid Mech. 430, 27–50.

Montiel, F., Bennetts, L.G., Squire, V.A., 2012. The transient response of floating elastic plates to wavemaker forcing in two dimensions. J. Fluids Struct. 28, 416–433.

Newman, J.N., 1985. Algorithms for the free-surface green function. J. Engrg. Math. 19, 57–67.

Newman, J.N., 1994. Wave effects on deformable bodies. Appl. Ocean Res. 16, 47–59.

Noad, I., Porter, R., 2017. Modelling an articulated raft wave energy converter. Renew. Energy 114, 1146–1159.

Noblesse, F., 1982. The green function in the theory of radiation and diffraction of regular water waves by a body. J. Engrg. Math. 16, 137–169.

Peter, M.A., Meylan, M.H., 2004. Infinite-depth interaction theory for arbitrary floating bodies applied to wave forcing of ice floes. J. Fluid Mech. 500, 145–167.

Porter, R., 2016. Surface wave interaction with rigid plates lying on water. Wave Motion 66, 118–131.

Porter, R., 2019. The coupling between ocean waves and rectangular ice sheets. J. Fluids Struct. 84, 171–181.

Porter, D., Porter, R., 2004. Approximations to wave scattering by an ice sheet of variable thickness over undulating bed topography. J. Fluid Mech. 509, 145–179.

Ren, K., Wu, G.W., Yang, Y.F., 2024. Surface wave interaction with floating elastic plates in channels. Phys. Fluids 36, 017143.

Renzi, E., 2016. Hydroelectromechanical modelling of a piezoelectric wave energy converter. Proc. R. Soc. Lond. Ser. A Math. Phys. Eng. Sci. 472, 20160715.

Renzi, E., Dias, F., 2012. Resonant behaviour of an oscillating wave energy converter in a channel. J. Fluid. Mech. 701, 482–510.

Renzi, E., Dias, F., 2013. Hydrodynamics of the oscillating wave surge converter in the open ocean. Eur. J. Mech. B Fluids 41, 1–10.

Renzi, E., Michele, S., Zheng, S., Jin, S., Greaves, D., 2021. Niche applications and flexible devices for wave energy conversion: A review. Energies 14, 6537.

Singh, M., Gayen, R., 2023. Mathematical study on the potential flow past a vertical submerged flexible plate of non-uniform thickness. J. Fluids Struct. 116, 103795.

Watanabe, E., Utsunomiya, T., Wang, C., 2004. Hydroelastic analysis of pontoon-type VLFS: a literature survey. Eng. Struct. 26, 245–256.

Xie, C., Choi, Y., Rongére, F., Clément, A.H., Delhommeau, G., Babarit, A., 2018. Comparison of existing methods for the calculation of the infinite water depth free-surface green function for the wave–structure interaction problem. Appl. Ocean Res. 81, 150–163.

Yang, Y., Ren, K., Zhou, B., Sun, S.Y., Huang, L., 2024. Wave interaction with multiple adjacent floating solar panels with arbitrary constraints. Phys. Fluids 36, 037121.

Zhao, W., Molin, B., Wang, Y., Wolgamot, H.A., Taylor, P.H., 2022. Nonlinear harmonics of gap fluid resonance with floating body motions. J. Fluid Mech. 951, A23.

Zheng, S., Meylan, M.H., Greaves, D., Iglesias, G., 2020. Water-wave interaction with submerged porous elastic disks. Phys. Fluids 32 (4), 047106.